

Asteroid 2023 NT1: A Cautionary Tale

Brin K. Bailey^{1a}, Alexander N. Cohen^{1b}, Dharv Patel¹, Philip Lubin^{1c}, Mark Boslough², Darrel Robertson³, Sasha Egan⁴, Jeeya Khetia¹, Teagan Costa¹, Elizabeth Silber⁵, Irina Sagert⁶, Oleg Korobkin⁶, Glenn Sjoden⁷

¹University of California - Santa Barbara, Broida Hall, Santa Barbara, California, 93106, United States

²University of New Mexico, 1700 Lomas Blvd, NE, Suite 2200, Albuquerque, New Mexico, 87131, United States

³NASA Ames Research Center, Moffett Field, California, 94035, United States

⁴New Mexico Institute of Mining and Technology, Energetic Materials Research and Testing Center, Socorro, New Mexico, 87801, United States

⁵Sandia National Laboratories, Albuquerque, New Mexico, 87123, United States

⁶Los Alamos National Laboratory, Los Alamos, New Mexico 87544, United States

⁷University of Utah, Salt Lake City, Utah 84112, United States

[a](mailto:brittanybailey@ucsb.edu)brittanybailey@ucsb.edu, [b](mailto:ancohen@ucsb.edu)ancohen@ucsb.edu, [c](mailto:lubin@ucsb.edu)lubin@ucsb.edu

Abstract – We investigate a variety of short warning time, terminal mitigation scenarios via fragmentation for a hypothetical impact of asteroid 2023 NT1, a Near-Earth Object (NEO) that was discovered on July 15, 2023, two days after its closest approach to Earth on July 13. The asteroid passed by Earth within ~ 0.25 lunar distances with a closest approach distance of $\sim 10^5$ km and speed of 11.27 km/s. Its size remains largely uncertain, with an estimated diameter range of 26 – 58 m and probable diameter estimate (weighted by the NEO size frequency distribution) of 34 m (JPL Sentry, September 12, 2023). The asteroid approached Earth from the direction of the Sun, as did both the Chelyabinsk asteroid in 2013 and comet NEOWISE in 2021. As a result, 2023 NT1 remained undetected until after its closest approach. If it had been on a collision course, it would have had an impact energy of ~ 1.5 Mt (assuming a spherical asteroid with the probable diameter estimate of 34 m, 2.6 g/cm^3 uniform density, and impact speed of 15.59 km/s). 2023 NT1 represents a threat that could have caused significant local damage ($\sim 3x$ Chelyabinsk airburst energy). We utilize the PI (“Pulverize It”) method for planetary defense to model potential mitigation scenarios of an object like 2023 NT1 through simulations of hypervelocity asteroid disruption and atmospheric ground effects for the case of a terminal defense mode. Simulations suggest that PI is an effective multimodal approach for planetary defense that can operate in extremely short interdiction modes (with intercepts as short as hours prior to impact), in addition to long interdiction time scales with months to years of warning. Our simulations support the proposition that threats like 2023 NT1 can be effectively mitigated with intercepts of one day (or less) prior to impact, yielding minimal to no ground damage, using modest resources and existing technologies.

1. Introduction

PI ("Pulverize It") is a proposed method of planetary defense which is intended to operate in both terminal and extended interdiction modes, representing a fundamentally different approach to threat mitigation [1]. Planetary defense has traditionally focused on mitigation via orbital modification or deflection, utilizing momentum transfer to prevent an impact. Deflection is applied in a range of techniques, from impulsive methods like direct impact (e.g., the Double Asteroid Redirection Test (DART)) [2] or nuclear ablation [3], to gradual orbit deflection (e.g., via surface albedo alteration) [4], or to the utilization of gravity tractors [5], ion engines, laser ablation, and further technologies [6]. PI is an alternative approach which would enable vastly shorter response times (if needed) and the ability to mitigate very large (up to ~ 1 km) threats using minimal launch mass in comparison to other mitigation methods, presenting the potential for significant reduction of both response time and launch mass. PI uses an array of hypervelocity kinetic penetrators (pions) that disassemble an asteroid or small comet into many small (typically < 10 m) fragments (Figure 1). Depending on the time scale of interception,

the fragment cloud either misses Earth entirely (long-warning time) or is dissipated in Earth's atmosphere (short-warning time, henceforth referred to as the "terminal mode"). The latter results in a series of airburst events with spatial and temporal spread at varying altitudes above 30 km. This highly de-correlates and distributes the energy of the parent asteroid, as individual fragment bursts as experienced by any observer are dispersed by time intervals that are longer than the blast wave pulse duration for each airburst.

In the terminal mode (hours-to-days intercept; 15 – 100 m diameter threats), the impacting fragment cloud disperses the energy relative to the unmitigated case. During atmospheric entry of the fragments, the high-speed ram pressure (or stagnation pressure) exerted by the atmosphere eventually exceeds the yield strength of the fragments, initiating a cascading breakup event. The ram pressure is determined by the density of the atmosphere and speed of the parent asteroid, whereas yield strength (or compressive strength) depends on the internal structure and integrity of the asteroid, including the strength of its components. As the pressure buildup on the fragment increases, it undergoes plastic deformation and begins to flatten and expand, a process commonly referred to as "pancaking" [1]. Continued flattening and expansion further increases the surface area on which the rising aerodynamic drag can act; this runaway process eventually converts the fragment's kinetic energy into a release of heat and pressure through detonation, or



Figure 1. Illustration of a launch vehicle delivering an array of hypervelocity kinetic penetrators to a threat, disassembling the asteroid into many small (generally < 10 m) fragments that enter Earth's atmosphere and airburst at altitudes > 30 km (terminal mode). This effectively spatially and temporally distributes the energy of the parent asteroid and yields ground effects that are vastly less destructive than effects from an equal unmitigated threat.

“bursting,” of the fragment [7]. These airbursts yield de-correlated shock waves and optical pulses on the ground (hereafter referred to as “ground effects”) which result in little to no damage.

In long warning time scenarios (>100 day intercept), the fragment cloud is spatially and temporally spread wide enough to miss Earth entirely, removing the threat. For mitigation of very large threats with long-term warning, PI can also be used in an enhanced deflection mode wherein the imparted energy is used to internally generate significant momentum transfer via large mass ejection. The fragments in this case have different orbits than the original center of mass, allowing them to miss Earth. In such long-term warning scenarios, the launch mass required for PI is much less than is needed for deflection missions for the same threat [1]. While this work aims to be synergistic with deflection methods, this point is important to note in reduction of cost and resources when designing mitigation scenarios.

1.1 Threat detection

A critical part of any mitigation system is the ability to detect threats in a timely manner. While we have reasonably long detection times for large threats (>1 km), we have poor situational awareness for the smaller asteroids (< 200 m diameter) that constitute the most common threats in the solar system. With a power law of threat incidence versus diameter and a lower limit on what are considered “significant” threats of about 20 m diameter for rocky compositions, we are severely limited in situational awareness in the smaller threat regime. It can be argued that this issue has two solutions, which are separate in approach but equal in goal: small-threat situational awareness can be 1) improved by heightened detection efforts and 2) augmented by establishment of effective short-term mitigation systems. Both phases could theoretically be improved concurrently to expedite our development of a robust planetary defense program.

1.2 Threat mitigation

Mitigation of a threat by using PI in a terminal mode consists of two stages: 1) interception and fragmentation of the asteroid and 2) dissipation of the fragment cloud through airbursts in Earth’s atmosphere. For terminal interdiction scenarios, the primary mechanism for threat mitigation is the distribution of the asteroid’s energy into spatially and temporally de-correlated ground effects.

The dynamics of hypervelocity interception of a threat are modeled in 2D and 3D using Livermore equation-of-state (LEOS) material models which include shock response and material vaporization and ionization. These simulations utilize Lawrence Livermore National Laboratory’s (LLNL) Arbitrary Lagrangian–Eulerian three-dimensional (ALE3D) hydrodynamics code [8], which is run through the High-End Computing Capability (HECC) at NASA Ames Research Center. This process rapidly converts the penetrator’s kinetic energy (in the asteroid reference frame) into heat and shock waves in the asteroid. The energy of the penetrator impact is enough to locally vaporize and ionize material near the impact site, while the generated shock waves damage and fracture the asteroid material as they propagate and reflect/refract. The expanding region of vaporized material imparts enough energy to the bulk of the asteroid to then drive the fragments apart with enough kinetic energy to overcome the

asteroid’s gravitational binding energy. See Section 3 below, as well as [1], [9], and [10] for more information regarding our hypervelocity impact simulations.

In the terminal mode, dissipation of the fragment cloud’s energy in Earth’s atmosphere yields two key ground effects: optical pulses (flashes) and acoustic blast waves (shockwaves). Ground effects simulations are conducted to analyze the optical and acoustic effects of each fragment airburst as perceived by an observer on Earth’s surface; see Section 4 below, as well as [1] and [10] for more information on our ground effects simulations. To design mitigation scenarios with acceptably low damage, we introduce damage thresholds for these effects. We utilize conservative metrics to limit the maximum optical energy output of any fragment to be below the combustion point for dry grass/paper (~ 200 kJ/m²) [11] and to keep all blast wave over-pressures (including contributions from caustics) from exceeding the threshold for residential window breakage (< 3 kPa) [12].

2. Asteroid 2023 NT1

2.1 Initial characterization

Little is known about asteroid 2023 NT1 with certainty, and it is important to note that the majority of parameters described here are estimates based upon very few well-constrained measurements. 2023 NT1 is classified as an Apollo Near-Earth Asteroid (NEA) and was first observed on July 15, 2023 using the M22 ATLAS-Sutherland telescope in South Africa [13]. The asteroid made its closest approach to Earth on July 13, 2023 at 10:13 (± 1 minute) TDB and passed at a distance of 0.00067 AU ($\sim 10^5$ km) (determined via a 3σ body target-plane error ellipse) with a speed of 11.27 km/s [14]. The body’s absolute magnitude (H ; defined as the apparent magnitude at 1 AU from the Sun and observer) was observed as 25.05 ($\sigma = 0.37706$) [14]. Observations of 2023 NT1 made by the Jet Propulsion Laboratory (JPL) and the International Astronomical Union (IAU) from July 15-September 16, 2023 yield an eccentricity of $0.51271 \pm 1.4427 \times 10^{-4}$ with an estimated orbital period of 949.58 ± 0.03919 days ($2.5998 \pm 1.0729 \times 10^{-4}$ years) [14]. At its closest approach, the asteroid was about 35 days past perihelion on its orbit around the sun with a semi-major axis of $1.8907 \pm 5.2018 \times 10^{-4}$ AU and an inclination of $5.7712 \pm 5.2018 \times 10^{-4}$ degrees [14].

While the body’s closest approach distance and speed and absolute magnitude are relatively constrained, the remainder of physical and orbital characteristics of 2023 NT1 are not known with certainty. Diameter estimates of the object are based on its absolute magnitude, yielding a size range of 26 – 58 m [14, 15]. JPL Sentry data estimates a probable size for 2023 NT1 by assuming a uniform spherical body with visual albedo $p_v=0.154$ (in accordance with the Palermo Scale) and weighting by impact probability and the NEO size frequency distribution to achieve a diameter estimate of 34 m, thought to be accurate to within a factor of 2 [15]. Assuming a spherical body with a 34 m diameter and uniform density of 2.6 g/cm³, the mass is roughly 5.2×10^7 kg, which is thought to be accurate to within a factor of 3 [15]. Assuming these characteristics, 2023 NT1’s mean impact energy is ~ 1.5 Mt.

2.2 Earth impact risk

Since the body has a non-zero inclination and a non-whole number ratio between the orbital period of Earth and the body, a future impact has very little chance of occurring. On September 16, 2023, JPL Sentry removed 2023 NT1 from its Impact Risk page, as additional observations ruled out previous potential impact estimates [15]. However, the conditions that gave rise to 2023 NT1's close passage without detection are an indication that existing planetary defense programs are not adequate for such short-term threats.

In relation to historical events, the diameter estimates of 2023 NT1 place the body between the size range of the Chelyabinsk meteor of 2013 (18 m diameter) and the Tunguska meteor of 1908 (estimated ~50 m diameter). Both events caused major disruptions to local human life and land; Chelyabinsk (which released energy equivalent to 0.57 ± 0.15 Mt TNT) injured over 1,600 people and damaged more than 7,000 buildings, resulting in an estimated \$33 million (1 billion rubles) of damage [16, 17, 18, 19]. The Tunguska event (which produced a yield of 3-50 Mt; most likely 3-15 Mt) flattened an area of 2,150 km² of forest and resulted in sparse fires out to 10-15 km from the epicenter [16, 17, 20, 21]. Objects at least the size of the Chelyabinsk asteroid are expected to impact Earth approximately every 50-100 years, while objects with the energy of the Tunguska asteroid are expected to impact Earth approximately every 300-1000 years (~300-500 years for an estimated 3-5 Mt event; ~800-1800 years for an estimated 10-15 Mt event) [22, 23, 17]. While future impacts of 2023 NT1 itself are unlikely, it is clear that Earth is vulnerable to such threats.

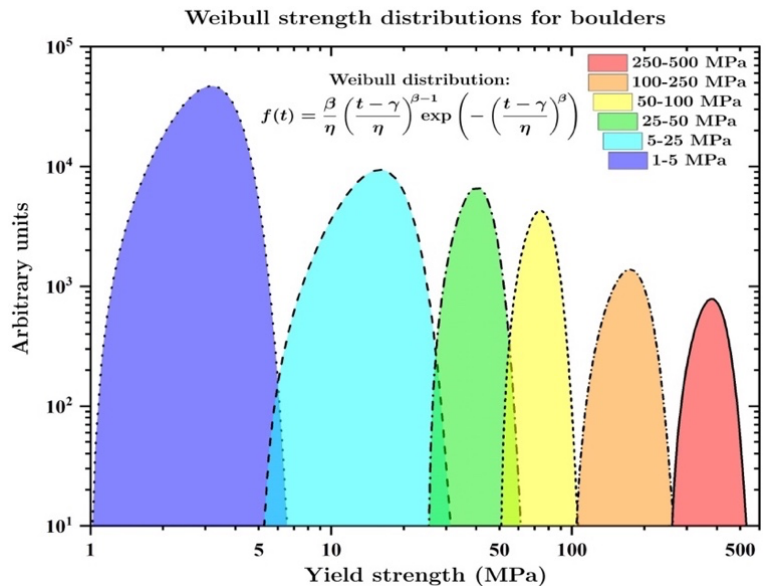
In the context of short-notice, large-scale potential threats, C/2020 F3 (comet NEOWISE) acts as an indicator of our need for heightened detection and short-timescale mitigation methods. NEOWISE is a long period comet of ~5 km diameter that was discovered by infrared (IR) telescope WISE on March 27, 2020, four months before its closest approach to Earth [24]. The sungrazer comet reached perihelion on July 3, 2020, passing about 0.295 AU from the Sun before making its closest approach to Earth on July 23 at a distance of 0.36 AU [25, 26]. With possible potential impact speeds (estimated from NEOWISE's orbit) ranging from ~50-70 km/s, the kilometer-scale comet could yield devastating results if an impact were to occur [26]. While NEOWISE is about 80-160 times larger than 2023 NT1, both undetected threats serve as clear warnings.

While 2023 NT1 currently poses no threat to Earth, it is conceivable that similar objects could go undetected and result in short-warning (or no-warning) impacts. In situations like these, deflection-based mitigation strategies fall short of preventing damage if warning times are not sufficiently long; the time taken to plan, assemble, launch, and deflect is likely to be on the scale of years, if not decades. To achieve an extensive planetary defense system, preparedness for a variety of threat scenarios—considering a large range of threat sizes and warning times—is imperative. It can be argued that a robust planetary defense system would be comprised of a layered system of reliable, tested methods for both detection and mitigation to achieve such preparedness. We explore this topic further in Section 5.

3. Interception and fragmentation

We model asteroids in the 20-50 m diameter range as heterogeneous rubble piles consisting of a distribution of spherical boulders of varying strengths embedded within a weak binder material. We include a porous crush model for both the binder and boulder materials, with 50% and 40% porosity, respectively. The binder has a weak mean strength of 25 Pa while the boulders range in strength from 1 – 500 mPa. Within each boulder and within the binder material, we vary the initial yield strength with a unique Weibull distribution (Figure 2). Given the uncertainty in the diameter of asteroid 2023 NT1, we simulate the interception of both a 20 m and a 50 m diameter case, each with 2.67 g/cm³ density. While it is estimated that asteroid 2023 NT1 would have had an Earth impact speed of 15.59 km/s, it is within reason to expect that current launch vehicles such as the SpaceX Falcon 9 (and similar vehicles) could deliver up to 2500 kg of payload mass to the target with characteristic energies C_3 of ~ 10 km²/s², resulting in a closing speed between the asteroid and the penetrator(s) of ~ 20 km/s. We use this value for all impact speeds in our hypervelocity impact simulations presented below. Note that the following simulations are a small subset of a much larger database of simulations we are in the process of developing for a wide range of threats.

Figure 2. Weibull strength distributions for the six boulder types in our rubble pile asteroid models. These distributions are normalized and used to initialize the yield strengths of the boulders, scaling up from 1 MPa initial yield strength. Additionally, a Weibull distribution is used for the binder material with a weak mean strength of 25 Pa. For reference, the violet 1–5 MPa distribution is comparable to hardened soil, the cyan 5–25 MPa distribution to standard grade concrete, the green 25–50 MPa distribution to high strength concrete, the yellow 50–100 MPa distribution to aluminum, the orange 100–250 MPa distribution to structural steel, and the red 250–500 MPa distribution to high strength steel and titanium. These strengths are an extremely conservative over-estimation of the strength of rubble pile asteroids.



3.1. Case 1: 20 m diameter with 100 kg penetrator

For our first hypothetical mitigation simulation, we simulate asteroid 2023 NT1 as a 20 m spherical asteroid with the heterogeneous material model described above. We find that an impact at 20 km/s with a 100 kg cylindrical tungsten penetrator with 10:1 L/D aspect ratio delivers a specific impact energy of ~ 3600 J/kg (defined as the kinetic energy of the impactor divided by the mass of the target), which is extremely effective at disrupting the 20 m asteroid to a size scale of < 5 m per fragment. Figure 3 shows the results of this simulation at $t = 5$ seconds after impact. As seen in the histograms, the mean fragment diameter is 1 m and the mean fragment speed is 9.3 m/s, which is > 1000 times the gravitational escape speed of the original asteroid.

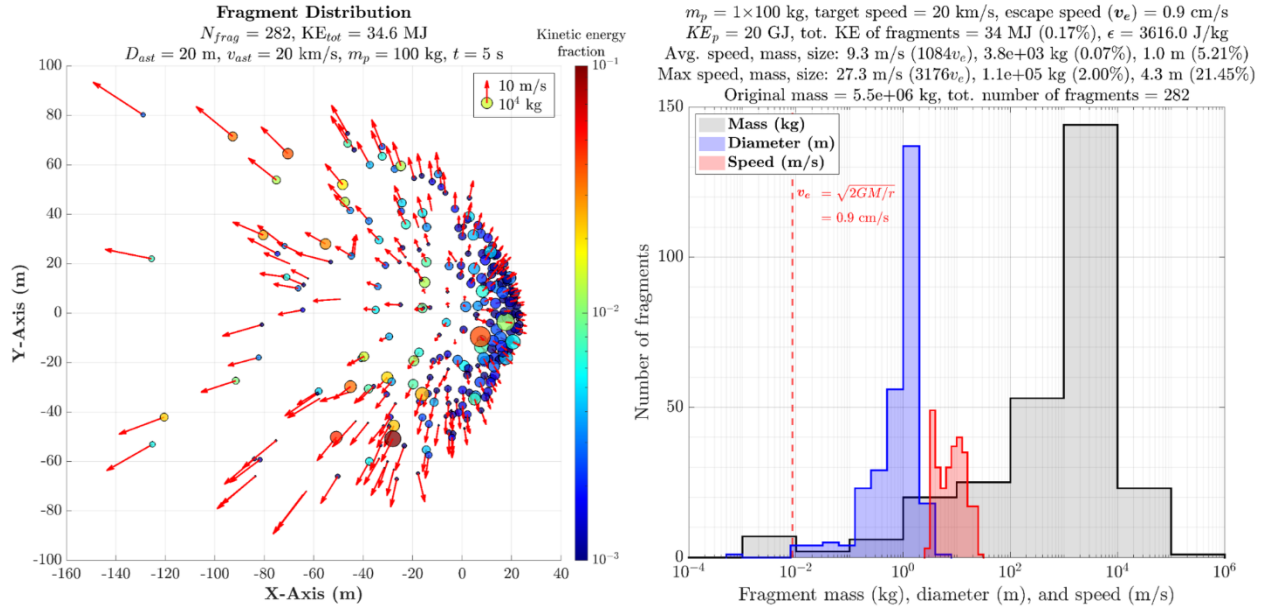


Figure 3: Fragment distribution and statistics at $t = 5$ seconds after impact for a 100 kg 10:1 aspect ratio tungsten cylindrical penetrator incident at 20 km/s upon a 20 m diameter rubble pile asteroid target. The black, blue, and red histograms indicate the distributions of fragment masses in kilograms, diameters in meters, and speeds in meters per second, respectively. Of note is the average fragment size of 1 m and average fragment speed of 9.3 m/s, which is over 1000 times greater than the gravitational escape speed of 0.9 cm/s (dashed red line on left). Also note that the maximum fragment size is 4.3 m, which is well below the 10 m acceptable fragment size threshold for rocky asteroid densities around 2.6 g/cm^3 [1, 2]. These results suggest that asteroid 2023 NT1, if similar to the Chelyabinsk asteroid in size and composition, can be mitigated using a single tungsten penetrator with mass on the order of 100 kg, assuming an asteroid closing speed of 20 km/s.

3.2 Case 2: 50 m diameter with 500 kg penetrator mass

By scaling the total penetrator mass from 100 kg to 500 kg, either in the form of a single 500 kg penetrator (1×500 kg case) or in the form of five 100 kg penetrators arranged in a x-shaped array (5×100 kg case), we find that we can achieve sufficient disruption of a 50 m analogue of asteroid 2023 NT1. The specific impact energy delivered in this case is ~ 1200 J/kg, which is still more than sufficient to disrupt the 50 m asteroid. Figure 4 shows a comparison between the two 500 kg cases described above and illustrates how concentrating the penetrator mass into a single 500 kg penetrator results in >2 times more efficient coupling of the penetrator kinetic energy to the bulk kinetic energy of the fragments after impact. This is likely due to the greater depth of penetration achieved by the 500 kg penetrator, which results in a greater tamping effect on the explosive expansion of the superheated material local to the impact site. However, both cases result in catastrophic disruption of the asteroid and mean fragment speeds which are >100 times the gravitational escape speed of the original asteroid.

As can be seen in Figure 4, there are a total of 1,010 fragments (≥ 1 m) at $t = 10$ seconds after impact in the 5×100 kg case, and 1,509 fragments (≥ 1 m) in the 1×500 kg case, but at 10 seconds after impact, both cases still exhibit a larger, more persistent fragment at the right edge. In both cases, this larger fragment is in the process of disassembling, which happens on timescales longer than 10 seconds, as evidenced by its rapid and continued deformation due to being composed of mostly completely failed material. Material in the failed state is only bound

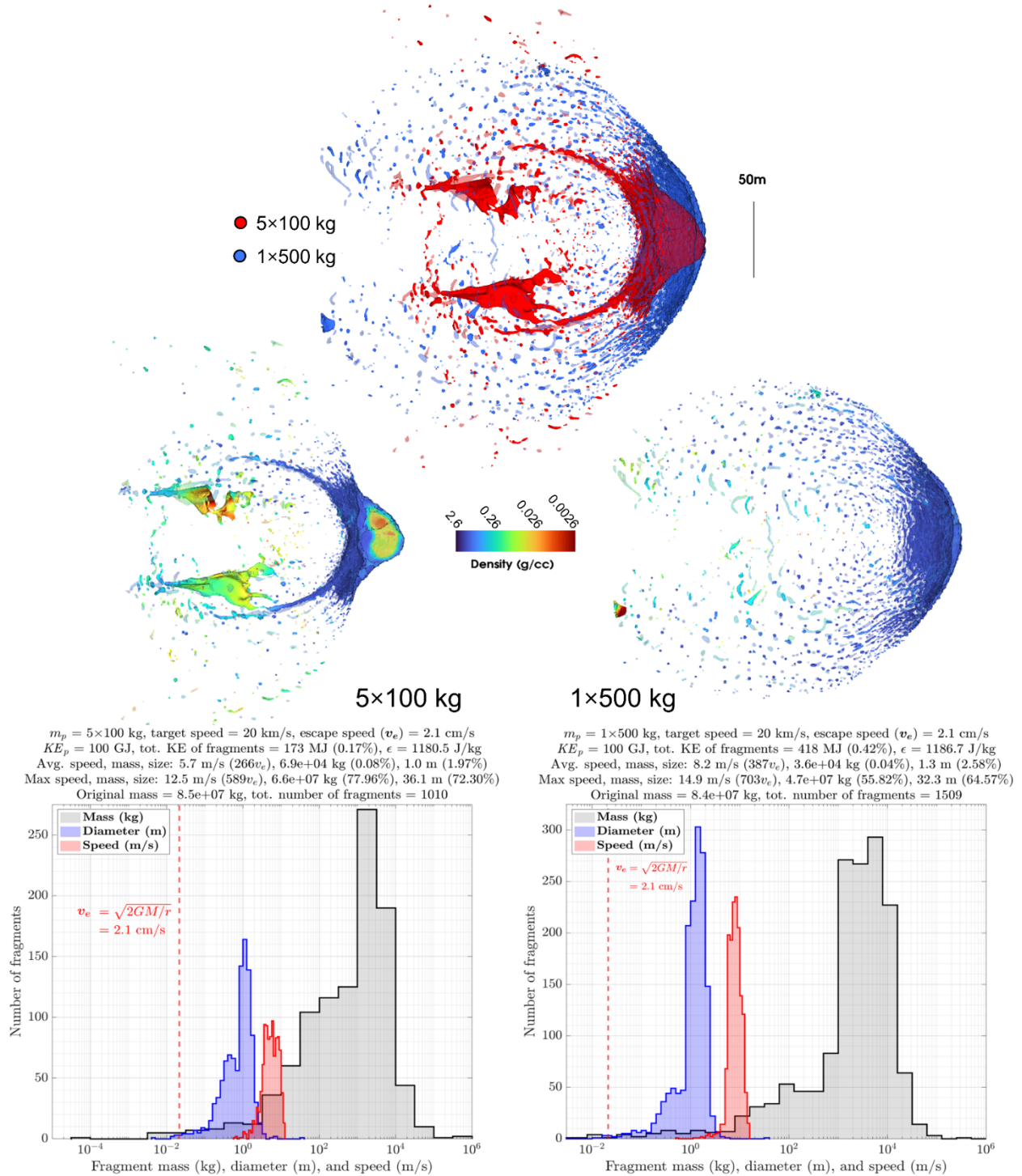


Figure 4: Fragment statistics at $t = 10$ seconds after impact for the $5 \times 100 \text{ kg}$ case (left) and the $1 \times 500 \text{ kg}$ case (right), both incident at 20 km/s upon identical 50 m diameter rubble pile asteroid targets. The black, blue, and red histograms indicate the distributions of fragment masses in kilograms, diameters in meters, and speeds in meters per second, respectively. The effectiveness of disruption can be quantified by comparing the 100 GJ initial kinetic energy of the penetrator(s) to the total kinetic energy of the fragments at a later time. In these cases, we see 0.17% of the original kinetic energy has been transferred to the fragments in the $5 \times 100 \text{ kg}$ case, and 0.42% has been transferred to the fragments in the $1 \times 500 \text{ kg}$ case, and it is clear from these results that the $1 \times 500 \text{ kg}$ case succeeds in transferring >2 times more of the initial kinetic energy of the penetrator than the $5 \times 100 \text{ kg}$ case.

by frictional cohesion and gravitational binding, which is greatly overcome by the fragment speeds induced by the impact. These reasons in combination lend credence to the hypothesis that the largest remaining fragment will dissociate into fragments of size comparable to the original interior boulder distribution, though likely even smaller due to the boulder material having been failed.

3.3 Comparison to DART impact results

Of interest is the comparison of our hypervelocity impact simulation results with the measured results of the Double Asteroid Redirection Test (DART) mission. DART successfully demonstrated momentum transfer to an asteroid via the controlled collision at ~ 6.1 km/s between a specially designed spacecraft (~ 580 kg at impact) and the asteroid Dimorphos, which has a diameter of ~ 168 m and orbits the larger asteroid Didymos as part of a binary system. The orbital period of Dimorphos was measured to have been shortened by 33.0 ± 1.0 minutes, corresponding to a change in its orbital speed of 2.70 ± 0.10 mm/s, ultimately suggesting a momentum multiplication factor of $\beta \approx 3.61$ if the densities of the two asteroids are presumed to be the same [27, 28]. Such momentum transfer enhancement is achieved by the ejection of material from the asteroid near the impact site. A recent study by Jewitt et al. analyzes ~ 40 boulders ejected from

Dimorphos as a result of the DART impact and finds a maximum boulder size of 7 m, while the majority of boulders have diameters less than 4 m; these correspond to a similar power-law distribution of boulder sizes measured on the surface of Didymos [29]. It is important to note that there is currently no evidence that the boulders ejected from Dimorphos by the DART impact were the result of further fragmentation. Rather, the boulders exist in a very similar size

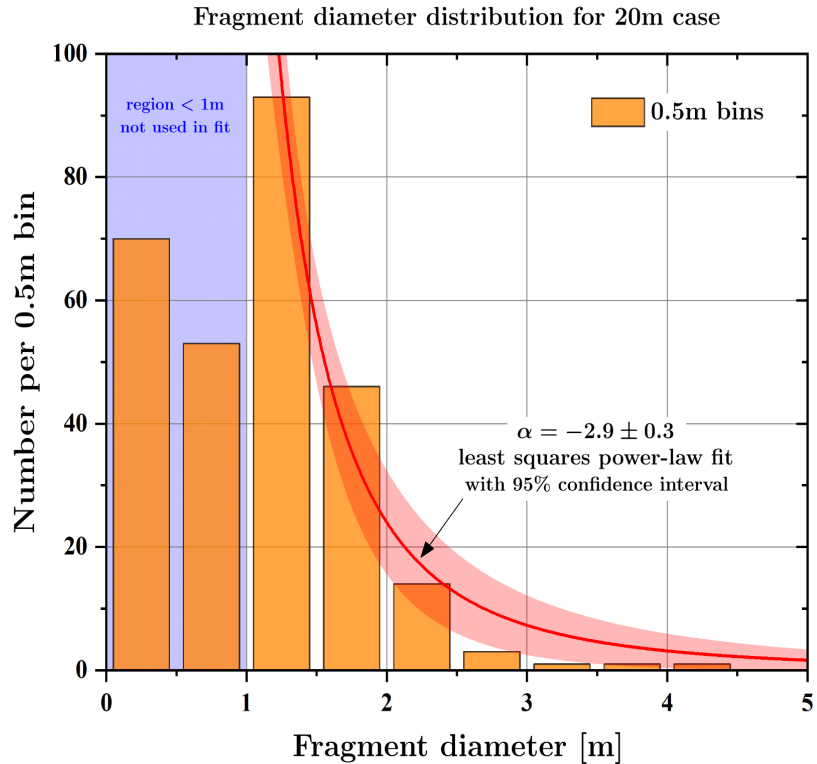


Figure 5: Fragment diameter distribution at $t = 5$ seconds after impact of a 100 kg penetrator at 20 km/s on a 20 m target, as shown in Figure 3. Disregarding fragment sizes below the 1 m³ mesh resolution of the simulation, we find a fragment diameter distribution which is remarkably similar to that measured by Jewitt et al. of the boulders ejected from Dimorphos after the DART impact [29]. A least-squares fit yields a power law $N \propto D^{-2.9}$, where D is the fragment diameter, or a differential size index of $q \approx -3.9$. This size distribution is also similar to that of the boulders present on the surface of Didymos, the larger of the two asteroids in the binary system. This is surprising since the impact velocities in the two cases are quite different (~ 6 km/s for the DART impact and 20 km/s for the simulated hypervelocity impact) and suggests that the boulders on the surface of Dimorphos may have already existed in this distribution prior to impact.

distribution as they did prior to impact, which indicates that ejection was the dominant mechanism rather than fragmentation.

As can be seen in Figures 3 and 4, our hypervelocity penetrator intercept simulations of 20 km/s impacts on 20 m and 50 m analogues of asteroid 2023 NT1 predict similar maximum boulder sizes of <10 m, but much smaller average boulder sizes of order 1 m (Figure 5), likely due to the large difference in impact speed and kinetic energy transferred. This suggests that above a certain closing speed threshold, the impact energy is sufficient to disrupt the asteroid to fragment sizes smaller than the original boulder distribution.

It is interesting to note that while the mean size of the fragments in the 20 km/s penetrator simulations (PI) is smaller than that measured for the DART impact, the distributions are very similar, namely a power-law with differential size index $q \approx -3.9$ ($\alpha \approx -2.9$). This suggests that the boulder material of rubble pile asteroids (like Dimorphos) may already exist in this size distribution, perhaps due to this material being the product of past collision events.

4. Ground effects

We simulate the ground effects of a variety of hypothetical mitigation scenarios for 2023 NT1 via fragmentation using PI; see [1] and [10] for a more thorough description than provided here. Given the large uncertainty in the asteroid's physical characteristics (such as size, shape, and density), we investigate 100+ threat cases that vary both the body's physical parameters (size, average density, and entry angle relative to Earth's horizon) and mitigation parameters (number of fragments and intercept time); a summary of all cases can be found in Tables 1-2 in the Appendix. Each scenario is designed to keep the ground effects (as experienced by an arbitrary observer on Earth's surface) below certain thresholds to minimize ground damage. As such, we utilize the results of our hypervelocity impact simulations as proxies for mitigation parameters.

Following the histogram distributions for fragment size in Figures 3 and 4, we vary the total number of fragments to keep the average fragment size for each case at or below ~4 m in diameter (average fragment size over all mitigated cases = 3.88 m, Table 1 in Appendix). Note that several individual cases have average fragment sizes larger than 4 m; these represent extreme cases with a conservative number of fragments relative to the threat size. Such scenarios are included for comparison to other threat sizes; e.g., a 60 m asteroid with an average density of 2.6 g/cm³ and entry angle of 45° which is broken into 1000 fragments with a one-day intercept (case 75, Table 1 in Appendix) is included for comparison with 26 – 58 m asteroids with the same physical parameters and mitigation scenario.

We introduce statistical variations in the fragmentation process to simulate the uncertainty in a real scenario by defining normal distributions for several fragment parameters, including diameter (fragment size), disruption speed (the asymptotic velocity at which fragments move away from the fragment cloud's center of mass, after having been decelerated by self-gravity of the asteroid), density, yield strength, and slant distance away from airburst. All scenarios assume a spherical target body. Mitigated scenarios assume an average fragment disruption speed of 1 m/s.

We also model the ground effects of unmitigated (i.e., unfragmented) scenarios as a comparison (Table 2 in Appendix). All unmitigated cases assume a spherical body with an entry angle of 45°. As the simulations show in the following sections, the damage to life and infrastructure caused by an unmitigated airburst is far greater than that of an equal mitigated case, the latter of which results in ground effects below estimated damage thresholds.

All scenarios, mitigated and unmitigated, assume an impact speed (the speed at atmospheric entry if an impact had occurred) of 15.59 km/s. This value, estimated by JPL Sentry [15], is approximated from 2023 NT1’s close approach speed of 11.27 km/s, with the additional contribution from Earth’s gravitational potential energy, assuming an impact of the asteroid. Thus, the scenarios outlined here simulate hypothetical outcomes if 2023 NT1 had hit Earth on its closest approach date of July 13, 2023, instead of narrowly missing.

4.1 Optical and acoustic ground effects

Upon interception and disassembly of the asteroid, its initial exo-atmospheric kinetic energy is distributed into the fragment cloud which, upon entry with Earth’s atmosphere, results in a series of airburst events. The energy of each fragment upon airburst is converted into optical and acoustic energies.

The conversion of kinetic energy into optical energy is highly dependent on fragment properties, particularly cohesive strength, and is poorly understood in general. We resort to measured optical data to model this conversion, primarily from Department of Defense satellite observations of a small number of relevant bolide sizes of interest to us (typically 1 – 15 m diameter) [12] [11].

Using an analytical extrapolation from [1], we calculate the optical energy flux at burst (in Joules) from E_{exo} as

$$E_{opt} = \left(\frac{E_{exo}}{8.2508} \right)^{1.13} \quad (1)$$

For the propagation of the optical pulse through the atmosphere, we use a full radiation transfer model to compute the optical power flux from each fragment at each observer. To model the optical pulses, we use a Monte-Carlo simulation technique with a simple Gaussian distribution to describe the power as a function of time produced by each fragment. By approximating the optical power distribution as Gaussian, the optical energy flux can be derived from the Gaussian integral; we then define the energy flux from an optical burst as observed on Earth’s surface based on an isotropic emitter.

The model includes atmospheric attenuation by approximating the parent asteroid as a blackbody source. Note that we assume an extremely conservative case of no cooling at the observer between fragment optical pulses. However, in a real scenario, fragments arrive on the order of tens of seconds apart (hundreds of seconds in some extreme cases) which would, in general, be enough time for significant cooling between bursts of incident optical energy. This will be important when judging the effectiveness of this method if the energy exceeds our threshold. A full explanation of the optical model can be found in [1] and [10].

The acoustic ground effects from an asteroid fragment airburst can be related to and approximated by those of nuclear blasts as discussed by Boslough et al. [30]; as such, we base our simulations of the acoustic ground effects from mitigation via PI on measurements of nuclear blasts. As the asteroid is hypersonic upon entry, a shock wave is created along the entire entry track until the burst phase, at which point we assume all remaining energy is dissipated into additional shock waves. To model the time evolution of the shock wave, we use a Friedlander functional form, given by

$$p(t, r) = p_0(r)e^{-t/t_1}(1 - t/t_1) \quad (2)$$

which describes the shock wave time evolution at a distance r with two free parameters: the peak pressure p_0 in Pa at time $t = 0$ seconds and the Friedlander positive pulse time scale, or zero crossing time, t_1 in seconds. Note that the time $t = 0$ seconds is the time at which the shock wave first arrives at the observer, not to be confused with the time at which the fragment bursts. We take an extrapolation of the t_1 parameter from [1], which is scaled by applicable measurements of nuclear airburst tests in [31, 12].

Letting ϵ denote the fraction of a 1 kt yield that goes into the blast wave (typically 0.5), we have $E_{nuc} = E_{ast-KT}/\epsilon$, where E_{ast-KT} is the asteroid airburst blast wave energy and E_{nuc} is the equivalent energy of a nuclear weapon [1]. Only a fraction of the nuclear weapon energy goes into the blast wave, while we conservatively assume that all the asteroid kinetic energy is fully transferred to the blast wave. The peak pressure at a distance r is calculated from the maximum pressure generated by a nuclear weapon of energy E_{nuc} (in kt) as

$$p(r) = p_n[rE_{nuc}^{-1/3}]^{\alpha_n} + p_f[rE_{nuc}^{-1/3}]^{\alpha_f} \quad (3)$$

where $p_n = 3.11 \times 10^{11}$ Pa is the pressure for a 1 kt standard weapon yield in the near field, $\alpha_n = -2.95$ is the power law index for the near field, $p_f = 1.80 \times 10^7$ Pa is the pressure for a 1 kt standard weapon yield in the far field, and $\alpha_f = -1.13$ is the power law index for the far field [1].

We simulate the airburst produced by each fragment as it enters Earth's atmosphere using (2) and (3). The model considers any interference between interacting shock waves, summing them to simulate the acoustic caustics. See [1] and [10] for a detailed description of the model in full.

The ground effects of unmitigated asteroids or very large (>20 m) fragments have the potential for significant destruction. Thus, our fragments are generally <10 m. For optical damage, there are two key effects to highlight: total energy deposition (J/m^2) and time-dependent power output (W/m^2). High energy deposition can lead to damage such as fires and skin damage (sunburn), whereas high power outputs can lead to temporary-to-permanent blindness. For acoustic damage, studies of window damage in atmospheric nuclear tests [12] have found that the threshold for residential window breakage corresponds to peak pressures of about 3 kPa. It is crucial to monitor both the optical and acoustic effects in designing proper mitigation scenarios with acceptably low damage.

For our simulations of 2023 NT1, we find that the ground effects of airbursts from mitigation via PI are kept below their respective damage thresholds (optical energy deposition under 200 kJ/m² for each burst and sum of all shock wave over-pressures under 3 kPa at any given ground point) and are vastly lower than their unmitigated counterparts. The magnitude of both effects increases as the parent asteroid size, speed, density, and/or entry angle increase; however, such factors can be counterbalanced by increasing the number of fragments and/or increasing intercept time prior to impact. To illustrate this, we plot the results of our ground effects simulations in the form of cumulative distribution functions (CDF) of both optical energy flux and acoustic over-pressure in the ground plane. We use the CDF of a particular threat scenario to determine whether that scenario results in ground effects of acceptably low magnitude. In addition to the maximum value, a useful metric is the 1% value of the CDF for a particular threat scenario, which is the magnitude at which 1% of ground locations resolved in the simulation experience optical energy flux or acoustic over-pressure above that value. We refer to this value henceforth as the 1% CDF value.

Simulations suggest that PI could effectively mitigate 2023 NT1 throughout our wide range of threat scenarios with very short warning times, from days to hours depending on physical characteristics. Assuming a worst-case scenario of a 60 m diameter iron-nickel asteroid with an average density of 7 g/cm³, an intercept two days prior to impact would be sufficient to keep the vast majority of ground effects below their respective damage thresholds, as indicated by the 1% CDF values of 61.5 kJ/m² for optical energy flux and 1.94 kPa for shockwave over-pressure (see Table 1 in Appendix). Additionally, for the same case, a 5-day intercept further reduces the optical and acoustic ground effect magnitudes, with 1% CDF values of 12.5 kJ/m² and 1.37 kPa (see Table 1 in Appendix).

4.3 Case 1: 34 m diameter scenarios

We highlight several 34 m diameter threat cases as proxies for the probable size estimate for 2023 NT1 [15]. For weak rubble-pile and granitic asteroids (average density of 1.4 – 2.6 g/cm³), we find that a one-day intercept prior to impact with an extremely conservative number of fragments (1000) is sufficient to keep all ground effects below their damage thresholds. Such a mitigation scenario with $\rho = 2.6$ g/cm³ yields 1% CDF values of 2.97 kJ/m² for optical energy flux and 0.436 kPa for shockwave over-pressure (Figures 6, 8, 9; Table 1 in Appendix). Extremely short time interdiction scenarios are also feasible; intercept times of 12 hours prior to impact yield reasonable effects (with shorter times likely viable as well) with 1% CDF values of 8.98 kJ/m² and 0.797 kPa (Figure 8; Table 1 in Appendix).

For strong stony to metallic asteroids (average density of 4.0 – 6.0 g/cm³), one-day intercepts remain feasible (Figure 9; Table 1 in Appendix). A 34 m threat with an average density of 6 g/cm³ and entry angle of 45° disassembled into 1000 fragments with a one-day intercept results in 1% CDF values of 21.2 kJ/m² and 1.28 kPa. However, longer intercepts and/or larger fragment numbers are preferred to decrease the magnitude of the ground effects.

For comparison, we estimate that an unfragmented spherical 34 m asteroid with an average density of 2.6 g/cm³ and entry angle of 45° would yield an average optical energy deposition of 80.2 kJ/m² and average acoustic over-pressure of 1.16 kPa as experienced on the ground, with 1% CDF values of 357. kJ/m² and 4.87 kPa, respectively (Figures 7, 8, 9; Table 2 in Appendix).

Figure 6. Optical (left) and acoustic (right) ground effects simulations showing a mitigation scenario of a 34 m asteroid (probable diameter estimate [15]) broken into 1000 fragments with a one-day intercept prior to impact. Simulations assume a spherical parent asteroid traveling at 15.59 km/s relative to Earth’s reference frame with an average density of 2.6 g/cm³, entry angle of 45°, and average fragment disruption of 1 m/s. Note that the current time in each simulation differs; the real-time of each simulation is seen in the title as “Time since first burst” (units of seconds), dictating the amount of time that has passed since the first airburst of the first fragment. The acoustic simulation also includes the time since the first shockwave arrived at the observer (which is represented by the green dot in both plots). **Left:** optical pulse simulation. Upper: real-time optical power flux. Middle: real-time optical energy flux. Lower: CDF dictating the frequency of occurrence of various energy flux values. Note that the total optical energy deposition is ~60 times lower than the damage threshold of 200 kJ/m², and less than 1% of locations on the ground experience > 3.44 kJ/m². **Right:** acoustic blast wave simulation. Upper: real-time pressure. Middle: maximum pressure experienced in each location throughout the current length of the simulation; each pixel displays the highest pressure it has experienced. Dark orange planes show the caustics (the positive interference from interacting shockwaves). Lower: CDF dictating the frequency of occurrence of various pressure values. Note that the sum of all shock wave over-pressures (including caustics) is ~2 times lower than the damage threshold of 2 kPa, and less than 1% of locations on the ground experience > 0.505 kPa. Higher pressures occur rarely as a result of two-point and three-point caustics.

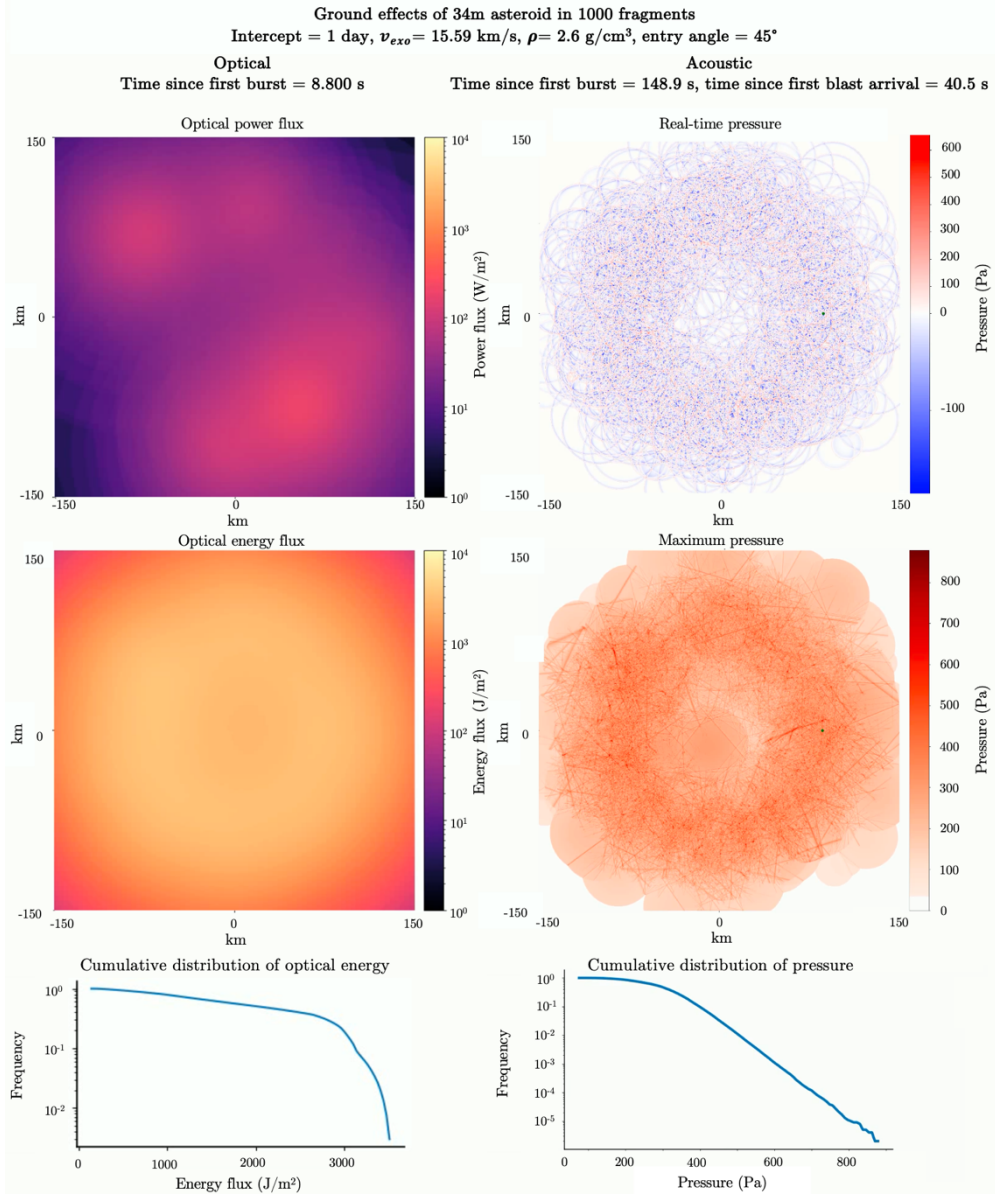
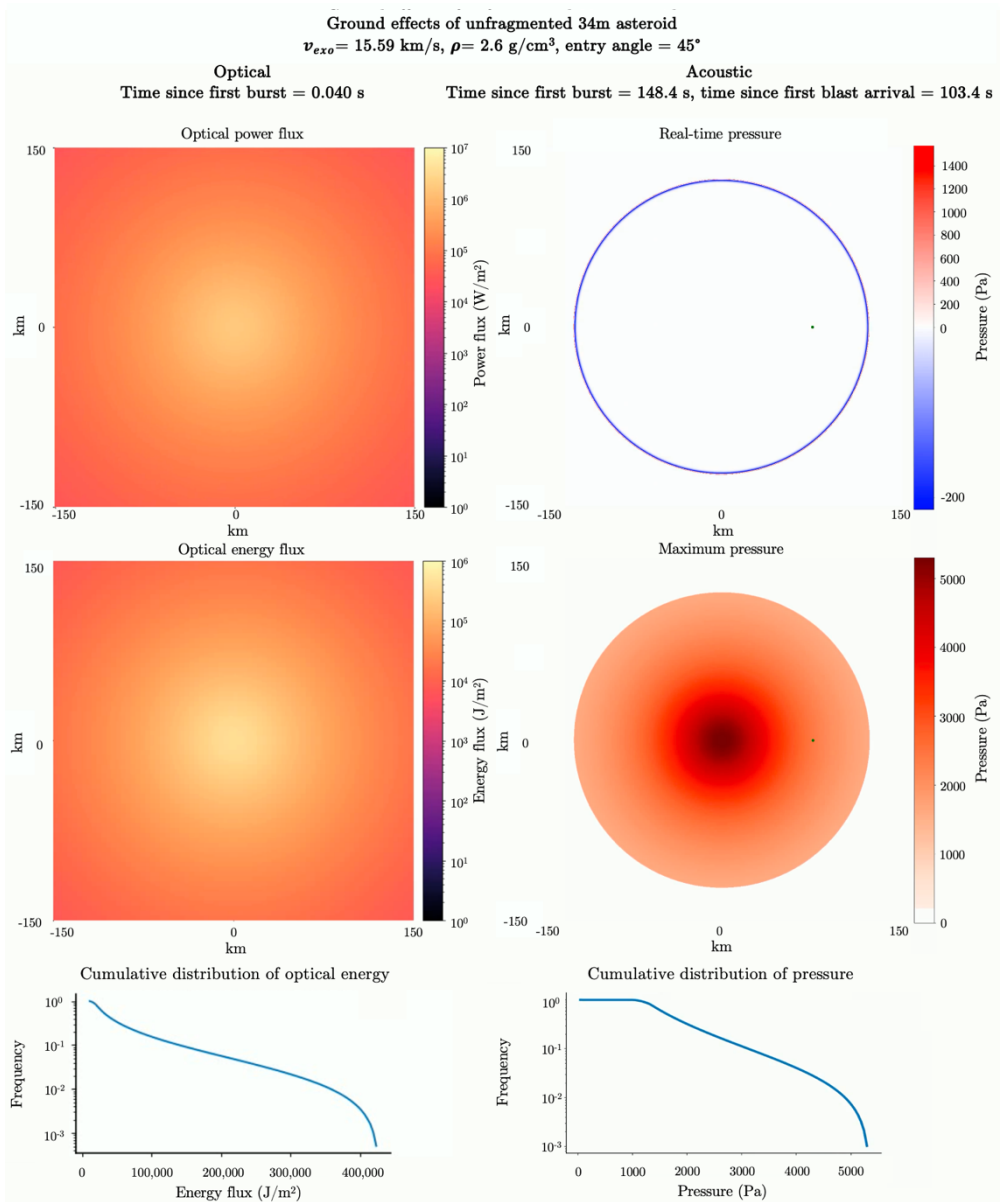


Figure 7. Optical (left) and acoustic (right) ground effects simulations showing an unmitigated (unfragmented) scenario of a 34 m asteroid (probable diameter estimate [15]). Simulations assume a spherical parent asteroid traveling at 15.59 km/s relative to Earth's reference frame with an average density of 2.6 g/cm³ and entry angle of 45°. Note that the current time in each simulation differs; the real-time of each simulation is seen in the title as "Time since first burst" (units of seconds), dictating the amount of time that has passed since the first airburst of the first fragment. The acoustic simulation also includes the time since the first shockwave arrived at the observer (which is represented by the green dot in both plots). **Left:** optical pulse simulation. Upper: real-time optical power flux. Middle: real-time optical energy flux. Lower: CDF dictating the frequency of occurrence of various energy flux values. Note that ~5.5% of locations on the ground experience an optical energy deposition greater than the damage threshold of 200 kJ/m²; 1% of ground locations experience 356 kJ/m². The total optical energy deposition is ~120 times higher than an equivalent scenario mitigated into 1000 fragments with a one-day intercept (Figure 6). **Right:** acoustic blast wave simulation. Upper: real-time pressure. Middle: maximum pressure experienced in each location throughout the current length of the simulation; each pixel displays the highest pressure it has experienced. Lower: CDF dictating the frequency of occurrence of various pressure values. Note that ~30% of locations on the ground experience shock wave overpressures greater than the damage threshold of 2 kPa; 1% of ground locations experience 4.87 kPa. The sum of shock wave over-pressures is ~6 times higher than an equivalent scenario mitigated into 1000 fragments with a one-day intercept (Figure 6).



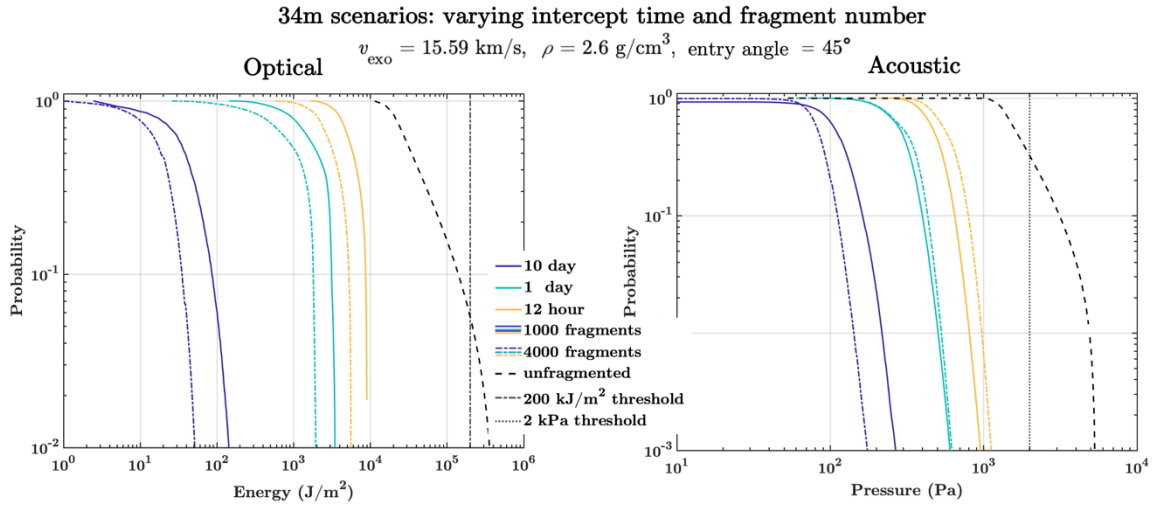


Figure 8. CDFs of the optical (left) and acoustic (right) ground effects of a variety of mitigation scenarios with a 34 m spherical parent asteroid. All scenarios assume an exo-atmospheric parent asteroid velocity (v_{exo}) of 15.59 km/s, average density (ρ) of 2.6 g/cm³, and entry angle of 45° relative to Earth’s horizon; mitigated scenarios assume an average fragment disruption speed (v_{dis}) of 1 m/s. The dash-dotted black line (left) and dotted black line (right) mark the optical and acoustic damage thresholds of 200 kJ/m² and a conservative 2 kPa, respectively. Legend dictates intercept time prior to impact, number of fragments, and scenario type (fragmented versus unfragmented).

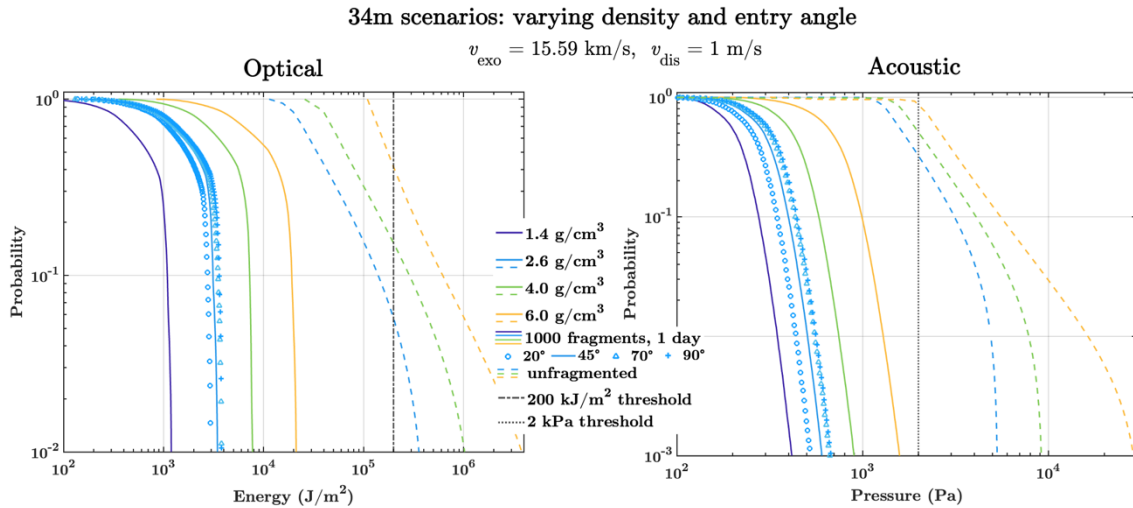


Figure 9. CDFs of the optical (left) and acoustic (right) ground effects of a variety of mitigated and unmitigated scenarios of a 34 m spherical parent asteroid with varying densities and entry angles. Unbroken exo-atmospheric energies range from 0.837 – 3.59 Mt. All scenarios assume an exo-atmospheric parent asteroid velocity (v_{exo}) of 15.59 km/s. All mitigated scenarios disassemble the parent asteroid into 1000 fragments with a one-day intercept prior to impact and assume an average fragment disruption speed (v_{dis}) of 1 m/s. All unmitigated scenarios (dashed lines) assume an entry angle of 45° relative to Earth’s horizon. The dash-dotted black line (left) and dotted black line (right) mark the optical and acoustic damage thresholds of 200 kJ/m² and a conservative 2 kPa, respectively. Legend dictates average density, entry angle relative to Earth’s horizon, and scenario type (fragmented versus unfragmented).

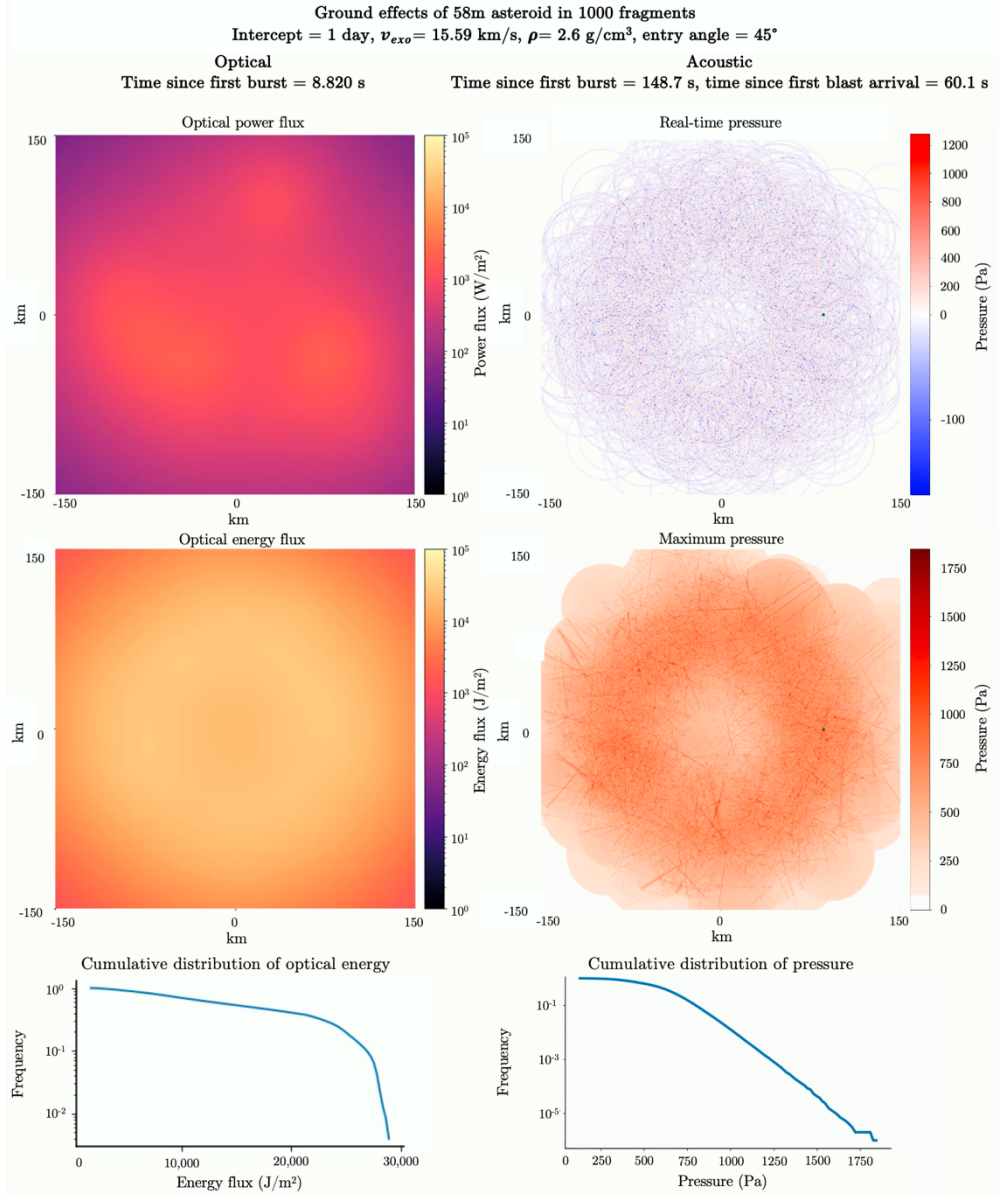
4.4 Case 2: 58 m diameter scenarios

To simulate higher-risk scenarios of 2023 NT1, we highlight several threats at the high-end diameter estimate of 58 m [15]. For weak rubble-pile to granitic asteroids (average density of 1.4 – 2.6 g/cm³), we find that a one-day intercept prior to impact with an extremely conservative number of fragments (1000) is sufficient to keep all ground effects below their damage thresholds. Such a mitigation scenario with $\rho = 2.6$ g/cm³ yields 1% CDF values of 28.7 kJ/m² for optical energy flux and 1.03 kPa for shockwave over-pressure (Figures 10, 12, 13; Table 1 in Appendix).

For strong stony to metallic asteroids (average density of 4.0 – 6.0 g/cm³), one-day intercepts are feasible, though 58 m asteroids with $\rho > 4.0$ g/cm³ may yield ground effects close to or slightly above the damage thresholds (Figure 13; Table 1 in Appendix). A 58 m threat with an average density of 6 g/cm³ and entry angle of 45° disassembled into 4000 fragments with a one-day intercept results in 1% CDF values of 105 kJ/m² and 2.25 kPa; for a 2-day intercept, these effects decrease, with 1% values of 35.0 kJ/m² and 1.4 kPa (Table 1 in Appendix).

For comparison, we estimate that an unfragmented spherical 58 m asteroid with an average density of 2.6 g/cm³ and entry angle of 45° would yield an average optical energy deposition of 1500 kJ/m² and average acoustic over-pressure of 3.47 kPa as experienced on the ground, with 1% CDF values of 6538 kJ/m² and 19.62 kPa, respectively (Figures 11, 12, 13; Table 2 in Appendix).

Figure 10. Optical (left) and acoustic (right) ground effects simulations showing a mitigation scenario of a 58 m asteroid (high-end diameter estimate [15]) broken into 1000 fragments with a one-day intercept prior to impact. Simulations assume a spherical parent asteroid traveling at 15.59 km/s relative to Earth’s reference frame with an average density of 2.6 g/cm³, entry angle of 45°, and average fragment disruption of 1 m/s. Note that the current time in each simulation differs; the real-time of each simulation is seen in the title as “Time since first burst” (units of seconds), dictating the amount of time that has passed since the first airburst of the first fragment. The acoustic simulation also includes the time since the first shockwave arrived at the observer (which is represented by the green dot in both plots). **Left:** optical pulse simulation. Upper: real-time optical power flux. Middle: real-time optical energy flux. Lower: CDF dictating the frequency of occurrence of various energy flux values. Note that the total optical energy deposition is ~7 times lower than the damage threshold of 200 kJ/m², and less than 1% of locations on the ground experience > 28.7 kJ/m². **Right:** acoustic blast wave simulation. Upper: real-time pressure. Middle: maximum pressure experienced in each location throughout the current length of the simulation; each pixel displays the highest pressure it has experienced. Dark orange planes show the caustics (the positive interference from interacting shockwaves). Lower: CDF dictating the frequency of occurrence of various pressure values. Note that the sum of all shock wave over-pressures (including caustics) is lower than the damage threshold of 2 kPa, and less than 1% of locations on the ground experience > 1.03 kPa. Higher pressures occur rarely as a result of two-point and three-point caustics.



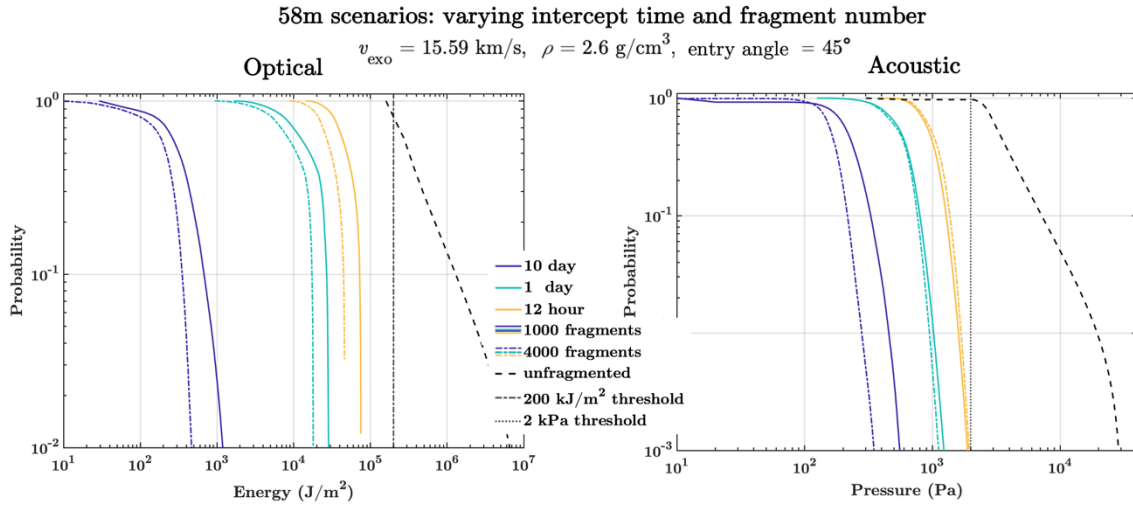


Figure 12. CDFs of the optical (left) and acoustic (right) ground effects of a variety of mitigation scenarios with a 58 m spherical parent asteroid. All scenarios assume an exo-atmospheric parent asteroid velocity (v_{exo}) of 15.59 km/s, average density (ρ) of 2.6 g/cm³, and entry angle of 45° relative to Earth’s horizon; mitigated scenarios assume an average fragment disruption speed (v_{dis}) of 1 m/s. The dash-dotted black line (left) and dotted black line (right) mark the optical and acoustic damage thresholds of 200 kJ/m² and 2 kPa, respectively. Legend dictates intercept time prior to impact, number of fragments, and scenario type (fragmented versus unfragmented).

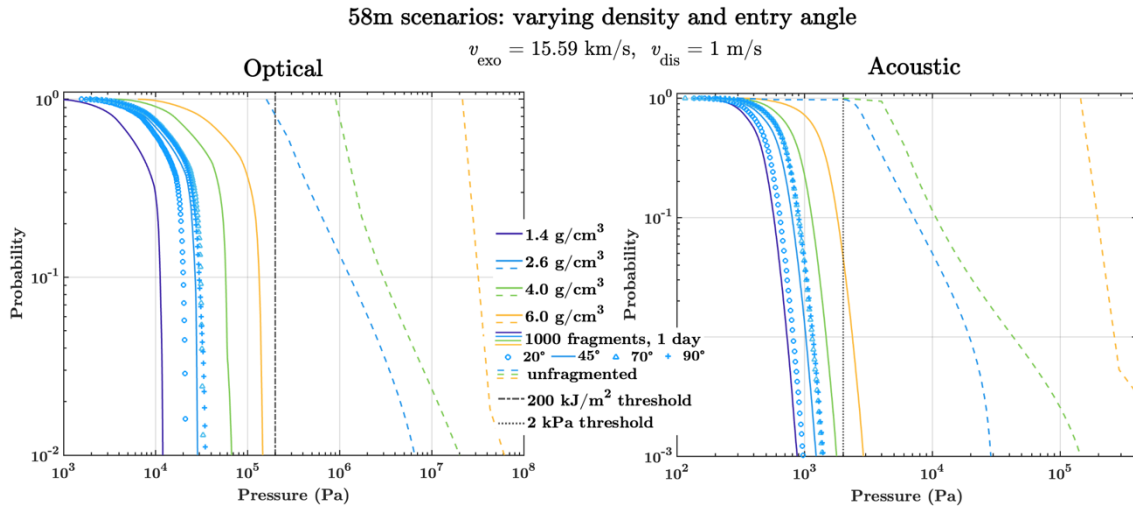


Figure 13. CDFs of the optical (left) and acoustic (right) ground effects of a variety of mitigated and unmitigated scenarios of a 58 m spherical parent asteroid with varying densities and entry angles. Unbroken exo-atmospheric energies range from 4.15 – 17.8 Mt. All scenarios assume an exo-atmospheric parent asteroid velocity (v_{exo}) of 15.59 km/s. All mitigated scenarios disassemble the parent asteroid into 1000 fragments with a one-day intercept prior to impact and assume an average fragment disruption speed (v_{dis}) of 1 m/s. All unmitigated scenarios (dashed lines) assume an entry angle of 45° relative to Earth’s horizon. The dash-dotted black line (left) and dotted black line (right) mark the optical and acoustic damage thresholds of 200 kJ/m² and 2 kPa, respectively. Legend dictates average density, entry angle relative to Earth’s horizon, and scenario type (fragmented versus unfragmented).

5. Discussion and future work

5.1 Summary of results

Based on the simulation results presented in the previous section, the PI method appears to be capable of mitigating short-notice threats like asteroid 2023 NT1 for a variety of potential threat characteristics, achieving reduced ground effects in comparison to equal unmitigated threats (Figure 14). This is illustrated in Figure 15, which shows a collection of the simulation results discussed prior for both the optical and acoustic ground effects. The 1% CDF values for optical energy flux (J/m^2) and acoustic overpressure (Pa) are useful metrics for comparing the effectiveness of a given mitigation scenario based on the magnitude of ground effects. Figure 15 shows that increasing the spatial and temporal distribution of the parent asteroid's energy by introducing more fragments or slightly longer intercept times keeps the 1% CDF values below acceptable thresholds for large-diameter and high-density threats. It stands to reason that these reduction methods could be achieved with a higher coupling of penetrator kinetic energy into bulk fragment kinetic energy via greater numbers of penetrators with greater mass and/or higher closing speed.

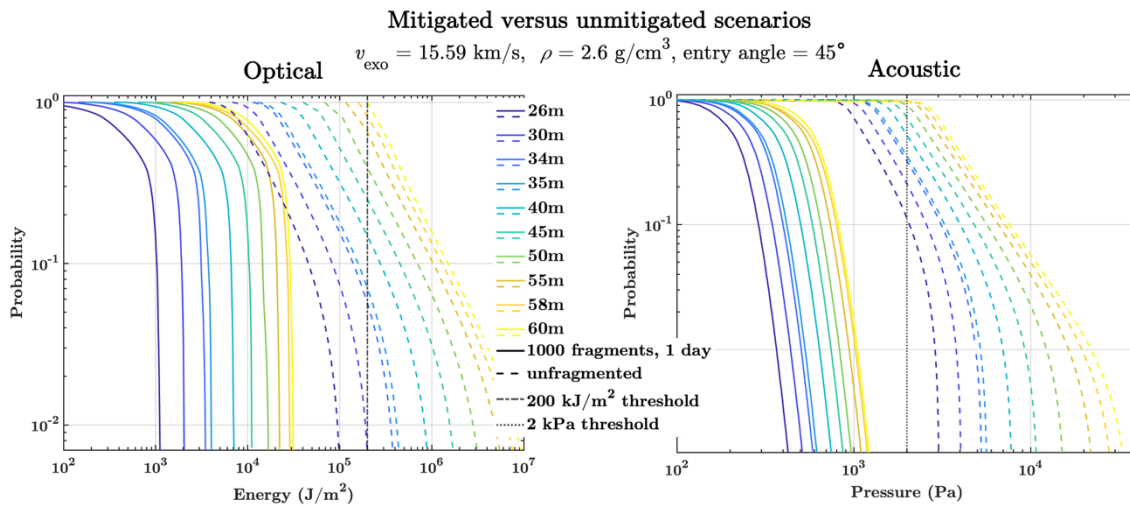


Figure 14. CDFs of the optical (left) and acoustic (right) ground effects for a variety of mitigation scenarios (solid lines) versus unmitigated scenarios (dashed lines). All scenarios assume a spherical parent asteroid with exo-atmospheric velocity (v_{exo}) of 15.59 km/s, average density (ρ) of 2.6 g/cm^3 , and entry angle of 45° relative to Earth's horizon; mitigated scenarios disassemble the asteroid into 1000 fragments with a one-day intercept prior to impact and assume an average fragment disruption speed of 1 m/s. The dash-dotted black line (left) and dotted black line (right) mark the optical and acoustic damage thresholds of 200 kJ/m^2 and 2 kPa, respectively.

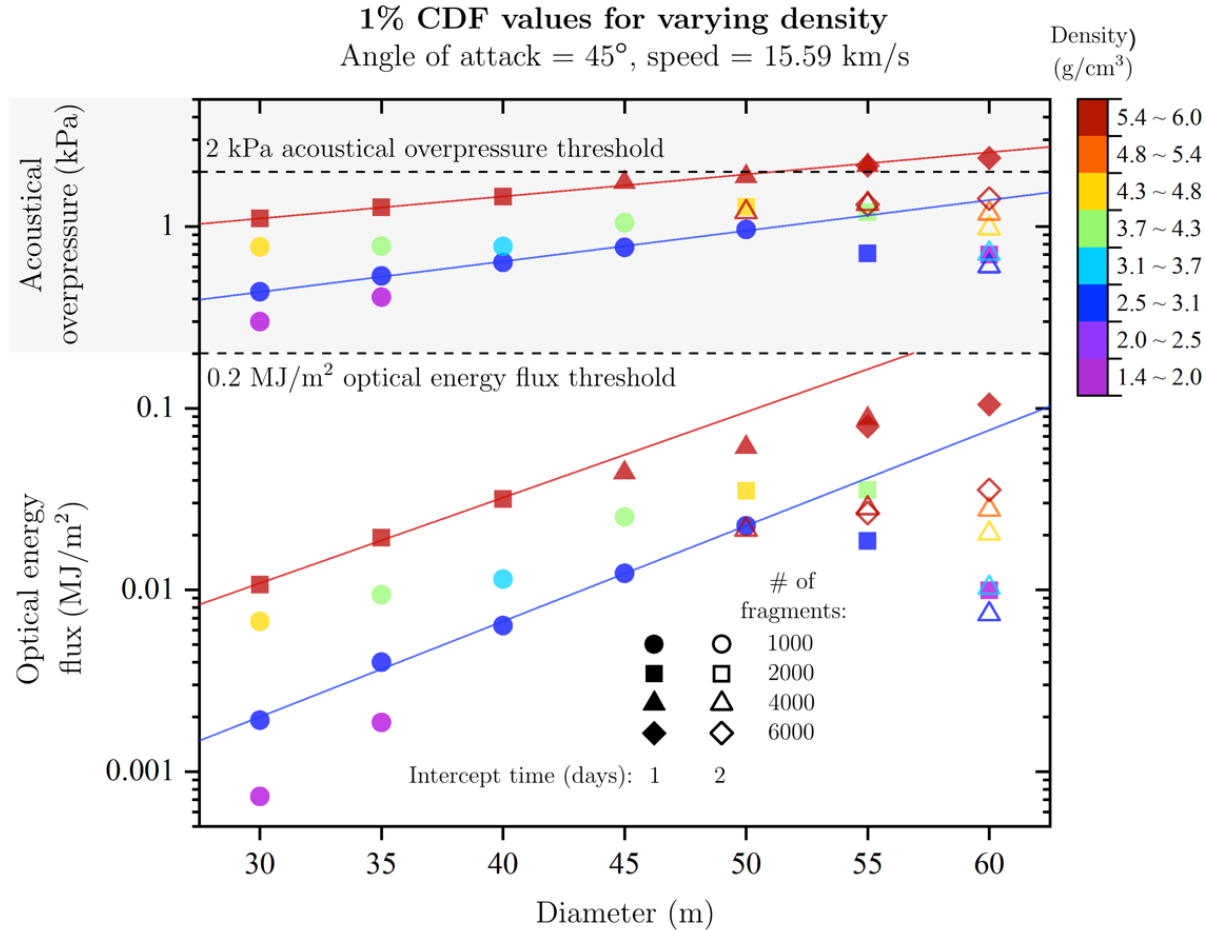


Figure 15. 1% CDF values for optical energy flux and acoustic over-pressure for asteroid 2023 NT1 mitigation scenarios with varying threat diameter (x-axis) and density (color scale). Points with filled symbols represent intercepts 1 day prior to impact, while open symbols represent 2-day intercepts, and the symbol type represents the number of fragments. Clear trends can be seen, as illustrated by the two fit lines in optical energy flux and acoustic over-pressure, which show that introduction of larger numbers of fragments and/or earlier intercept times are required to keep the 1% CDF values below the acceptable damage thresholds and the threat diameter and density is increased.

5.2 Limitations of the model

The results of these ground effects simulations in tandem with the hypervelocity impact simulations suggest that PI may be an effective strategy for mitigating objects like 2023 NT1. However, we acknowledge that our simulation results presented here represent a very limited range of potential threat scenarios which do not fully encompass a high-fidelity investigation of the PI method for all possible NEOs. Our analogues for 2023 NT1 assume spherical, rubble-pile asteroids within a small size range (20 – 60 m diameter) and with an impact speed of 15.59 km/s. While we vary threat parameters such as the average density (1.4 – 7.0 g/cm³) and entry angle (20° – 90°), it is important to note that the model presented here spans a limited range of the potential physical and impact parameters of 2023 NT1, or any other possible NEO. While our simulations not presented within this paper span asteroid sizes of 15 – 1000 m in diameter and with a variety of strength models, more work is needed to expand

the simulation regime to encompass a wider range of potential threat scenarios (see our website for an extended database at [10]).

Additionally, while our simulations suggest that asteroid disassembly via PI could mitigate the threat estimates presented here, this method has not yet been put into practice beyond simulations. An experimentation phase with testable methods that produces reliable, reproduceable results is imperative for a thorough analysis of PI. Further work is needed to establish physical experiments to test the stages of the method (e.g., impactor design and delivery via launch vehicles, hypervelocity impact of a comprehensive range of threat analogues, distribution of fragments, etc.) beyond a simulation phase.

5.3 Limitations of planetary defense

The results of these ground effects simulations in tandem with the hypervelocity impact simulations suggest that PI may provide an effective strategy for mitigating both terminal and long warning time threats. However, limitations to this method exist; a distinct constraint to mitigation is the necessity to observe a threat prior to its potential impact. The argument can be made that a foremost global detection system that enables full-sky, high-cadence situational awareness is a prerequisite to establishing a robust planetary defense system. Missions like the Rubin Observatory Legacy Survey of Space and Time (LSST) and NASA’s upcoming Near-Earth Object (NEO) Surveyor are imperative to the detection and cataloguing of potentially hazardous NEOs.

A full planetary defense system would encompass thorough and reliable methods for both detection and mitigation. Establishing numerable approaches to each aspect would create safeguards; e.g., supplementation of the ground-based Rubin Observatory LSST with a space-based instrument like NEO Surveyor that can better detect NEOs approaching from the direction of the Sun. We propose PI as a potential multimodal mitigation method not to replace other methods, but as a supplementary approach to bolster our response to potential threats. There is currently no planetary defense system that allows for short-warning mitigation. A robust planetary defense system would not be limited to a single mitigation strategy, but rather would be a highly redundant and layered system, akin to national defense systems. We envision PI as being synergistic with existing mitigation strategies, such as deflection, which may be logistically favorable in some threat scenarios (particularly those with especially long warning times).

5.4 When to deflect, fragment, or accept the hit

There exists a tradeoff between mitigation methods wherein different strategies may be favorable in different threat scenarios. Deflection methods, such as DART, can be useful for cases with very long warning times (decades to centuries). For decreased warning times, a fragmentation system like PI could be highly favorable. In comparing deflection to fragmentation, it is important to highlight two key metrics: method of transfer and threat scenario.

Deflection mitigates a threat through momentum transfer, whereas fragmentation via PI imparts energy transfer. These different transfer methods yield differences in mass needed off the launch pad. Broadly, the momentum transfer (assuming inelastic collision) applied by deflection (and

kinetic impact in general) is only part of the overall momentum change. For example, DART had an effective beta of $\beta \approx 3.61$; however, this parameter is highly dependent upon the target asteroid and cannot generally be assumed to be similar in other scenarios [2, 32]. To achieve the necessary momentum transfer, deflection generally requires a large launch mass. For fragmentation, energy transfer is imparted by penetrators that can be either passive or active (explosive) which penetrate the asteroid and cause shockwaves to propagate, inducing material failure upon early impact. The impactor then vaporizes both itself and the target material, forming a high-pressure gas/plasma cloud that expands rapidly, driving radial expansion and dissociating the target into fragments. Our simulations suggest that fragmentation could potentially be similarly effective to deflection in extended time scales, with the additional advantage of requiring less launch mass (Figure 16).

The question of which mitigation method is most favorable for a given scenario is extremely dependent on how well the object’s orbital and physical parameters are known (e.g., size, composition, yield strength; orbital path). The use of deflection—or any other mitigation method, particularly when used in advance—requires precise observation of the object’s orbital path to determine impact probability and warning time. Focusing our attention on 2023 NT1, objects observed with little to no warning time prior to their closest approach cannot yet be mitigated with certainty. Hypothetically, if 2023 NT1 was observed ahead of time and found to be on a collision course with Earth, how (and whether or not) to mitigate it would depend on our knowledge of its characteristics.

For terminal interdiction modes with warning times of hours to several days, it may be the case that fragmentation is a more feasible mitigation method. For 2023 NT1’s low-end diameter estimate, we estimate that deflection of a 26 m rubble pile asteroid with an average density of 2.6 g/cm^3 and velocity of 20 km/s (relative to Earth) using a one-day intercept prior to impact and a conservative miss distance of 4 Earth radii ($x = 4R_E$) would require ~ 200 metric tons of deflector mass (Figure 16). For the same scenario with a less conservative miss distance of 1 Earth radius, we estimate a deflector mass of ~ 50 metric tons. For 2023 NT1’s high-end diameter estimate of 58 m (assuming $\rho = 2.6 \text{ g/cm}^3$ and

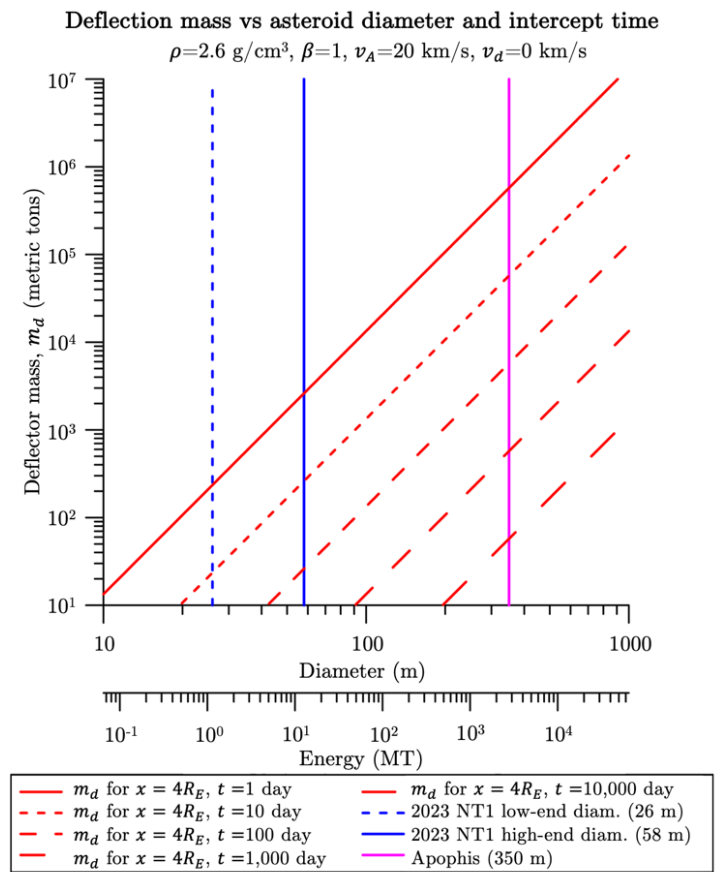


Figure 16. Deflector mass required for a completely inelastic momentum transfer via deflection for threats from 10 m to 1 km diameter for deflection times from 1 day to 10,000 days. Scenarios assume a spherical asteroid with average density (ρ) of 2.6 g/cm^3 and velocity (v_A) of 20 km/s and use a deflection miss distance of 4 Earth radii ($4R_E$).

$v_A = 20$ km/s), we estimate deflector masses of ~ 3000 metric tons for $x = 4R_E$ and ~ 750 metric tons for $x = R_E$ for one-day deflection intercepts (Figure 16). For mitigation via fragmentation of the same 26 m and 58 m asteroids with a one-day intercept prior to impact, our simulations suggest the threats could each be disassembled and mitigated by a single 100 kg penetrator (assuming a closing speed of 20 km/s).

Note that in order to achieve a scenario with a one-day intercept, the impactor (whether a deflector like DART or a penetrator for fragmentation like PI) would need to be launched several days in advance (dependent upon preferred miss distance). Additionally, the success of deflection is largely dependent upon the deflector's velocity vector relative to the asteroid's velocity vector. Assuming the capability to achieve a feasible launch mass for a one-day deflection intercept, a perpendicular impact would likely not provide enough momentum transfer to mitigate the threat.

With warning times on the order of one week or longer for small objects like 2023 NT1, deflection becomes more feasible; however, it may continue to be the case that fragmentation is potentially more effective while requiring less launch mass and potentially shorter launch times prior to impact (Figure 16) [1]. Using the same 26 m analogue for 2023 NT1 as above, we estimate that deflecting 10 days prior to impact would require deflector masses of ~ 20 metric tons for $x = 4R_E$ and ~ 5 metric tons for $x = R_E$; for the 58 m estimate, we find masses of ~ 300 metric tons and ~ 75 metric tons (Figure 16).

In regards to 2023 NT1 and similarly sized threats ($\sim 20 - 60$ m diameter), some may argue that mitigation of asteroids within this size range should be minimal, or perhaps unnecessary, depending on their impact location. Hypothetically, we introduce a scenario in which 2023 NT1 was observed with short warning and estimated to impact a large uninhabited area (e.g., large desert or mid-ocean). It can be argued that such an impact may leave human life and infrastructure unperturbed, thus making a mitigation effort redundant, or perhaps even harmful. It is possible that attempted mitigation of an otherwise potentially harmless impact could yield unintentional consequences; e.g., an unsuccessful deflection effort may push the object towards a habited area, or needless fragmentation could spread ground effects over a habited area.

For location-dependent terminal threat scenarios such as these, deciding how and if to mitigate is conditional upon how well the object's path is known. Given a situation in which there is near certainty that an asteroid will impact an uninhabited area and yield no damage, it may be reasonable to argue that the impact should occur unimpeded, or that fragmentation may be risky. However, the justification for such a risk is extremely dependent upon the level of knowledge of the threat. The asteroid's physical and orbital parameters should be extremely well-constrained, generally from continued and precise observation over time, which may not be possible for terminal scenarios with warning times of hours to days. The tradeoff between impact and terminal mitigation raises questions which have not yet been fully discussed within the field; further work is required to determine the boundary between potential outcomes.

Similarly, we introduce another scenario in which an asteroid is expected to impact an inhabited area that is close to an uninhabited area; e.g., an estimated impact over Los Angeles, CA. It could be argued that in such a scenario, a small-scale terminal deflection effort may successfully nudge the object into the Pacific Ocean, whereas mitigation via fragmentation could potentially

disperse fragments (and thus ground effects) over Los Angeles and/or surrounding inhabited areas. However, our results suggest that the ground effects from terminal-scenario fragmentation of asteroids in the smaller threat regime (<200 m diameter) are kept below the estimated damage thresholds mentioned above. Though, we note again that further work is needed to enact physical experimentation of fragmentation, and additional work is needed to determine the limit of justification for mitigation versus unimpeded impact.

6. Conclusions

Simulations suggest that PI is an effective approach for planetary defense that can operate in extremely short time scales in which other methods are not feasible, as well as in extended time scenarios to mitigate very large threats. This approach requires much less launch mass than other methods and potentially enables an extremely rapid response, testable method, and deployable approach using existing technologies. As analogues for 2023 NT1, our simulations suggest that rubble pile asteroids in the 20 – 50 meter-class can be effectively disrupted and fragmented via 20 km/s impacts with 100 and 500 kg 10:1 aspect ratio cylindrical tungsten penetrators. With such modest penetrator masses, the use of a SpaceX Falcon 9 (which has a payload capacity far greater than 500 kg), or a similarly capable launch vehicle, potentially enables the mitigation of a wide variety of asteroid threats well in excess of the 50 m asteroid simulated in this study. Our simulations suggest that for the case of asteroid 2023 NT1 with a variety of mitigated threat scenarios in the 26 – 60 meter-class, PI reduces the most likely ~1.5 Mt impact energy (assuming a spherical asteroid of 34 m diameter, 2.6 g/cm³ uniform density, and 15.59 km/s impact speed) [15] into dispersed optical pulses and shock wave over-pressures that result in minimal ground damage. The ground effects produced by the interaction of the fragment cloud with Earth's atmosphere are below acceptable thresholds, with the vast majority of optical energies below 200 kJ/m² and acoustic pressures below 3 kPa. A terminal solution for short-warning mitigation such as PI, implemented to work synergistically with deflection, could work to potentially establish a robust planetary defense system with multiple mitigation approaches. Such a system could be prepared for a wide variety of threat scenarios, particularly for regimes in which we currently lack complete situational awareness. Further work is needed to determine how the nature of a particular threat can dictate the most effective mitigation strategy, and a robust, global detection system is required to enable full-sky, high-cadence situational awareness.

7. Acknowledgements

We gratefully acknowledge funding from NASA NIAC Phase I grant 80NSSC22K0764, NASA NIAC Phase II grant 80NSSC23K0966, and NASA California Space Grant NNX10AT93H, as well as from the Emmett and Gladys W. Fund. We gratefully acknowledge support from the NASA Ames High End Computing Capability (HECC) group and Lawrence Livermore National Laboratory (LLNL) for the use of their ALE3D simulation tools used for modeling the hypervelocity penetrator impacts and for funding from NVIDIA for an Academic Hardware Grant for a high-end GPU greatly speeding up ground effect simulations. Sandia National Laboratories is a multi-mission laboratory managed and operated by National Technology & Engineering Solutions of Sandia, LLC (NTESS), a wholly owned subsidiary of Honeywell International Inc., for the U.S. Department of Energy's National Nuclear Security Administration (DOE/NNSA) under contract DE-NA0003525. This work was also supported by the Laboratory Directed Research and Development program of Los Alamos National Laboratory (LANL)

under project number 20220771ER. LANL is operated by Triad National Security, LLC, for the National Nuclear Security Administration of the U.S.DOE (Contract No. 89233218CNA000001). We would like to thank our large team of researchers and undergraduates, including Ruitao Xu, Ysabel Chen, Jasper Webb, Hannah Shabtian, Albert Ho, Alok Thakar, Alex Korn, Kellan Colburn, Daniel Bray, Kavish Kondap, and Jerry Zhang for their tireless work and enthusiasm to defend the planet.

8. Website and additional materials

Additional papers, simulations, and visualizations for the PI project, as well as information on our other projects, can be found on our website. Detailed simulations of the acoustic ground effects, optical ground effects, hypervelocity penetrator impacts, and further effects of the PI model can be found on our group YouTube channel, updated regularly.

- UCSB Deepspace website: www.deepspace.ucsb.edu
- PI project: www.deepspace.ucsb.edu/projects/pi-terminal-planetary
- UCSB Deepspace YouTube channel: www.youtube.com/@UCSBDeepspace

References

- [1] Lubin, P., 2023. PI -- Terminal Planetary Defense. [arXiv:2110.07559v14](https://arxiv.org/abs/2110.07559v14) [astro-ph.EP].
- [2] Rivkin, A.S., Chabot, N.L., Stickle, A.M., Thomas, C.A., Richardson, D.C., Barnouin, O., Fahnestock, E.G., Ernst, C.M., Cheng, A.F., Chesley, S., Naidu, S., Statler, T.S., Barbee, B., Agrusa, H., Moskovitz, N., Daly, R.T., Pravec, P., Scheirich, P., Dotto, E., Corte, V.D., Michel, P., Küppers, M., Atchison, J., Hirabayashi, M., 2021. The Double Asteroid Redirection Test (DART): Planetary Defense Investigations and Requirements. *Planet. Sci. J.* 2, 173. <https://doi.org/10.3847/PSJ/ac063e>
- [3] Dearborn, D.S.P., Bruck Syal, M., Barbee, B.W., Gisler, G., Greenaugh, K., Howley, K.M., Leung, R., Lyzhoft, J., Miller, P.L., Nuth, J.A., Plesko, C.S., Seery, B.D., Wasem, J.V., Weaver, R.P., Zebenay, M., 2020. Options and uncertainties in planetary defense: Impulse-dependent response and the physical properties of asteroids. *Acta Astronaut.* 166, 290–305. <https://doi.org/10.1016/j.actaastro.2019.10.026>
- [4] Hyland, D.C., Altwaijry, H.A., Ge, S., Margulieux, R., Doyle, J., Sandberg, J., Young, B., Bai, X., Lopez, J., Satak, N., 2010. A permanently-acting NEA damage mitigation technique via the Yarkovsky effect. *Cosm. Res.* 48, 430–436. <https://doi.org/10.1134/S0010952510050096>
- [5] Mazanek, D.D., Reeves, D.M., Hopkins, J.B., Wade, D.W., Tantardini, M., Shen, H., 2015. Enhanced Gravity Tractor Technique for Planetary Defense. Presented at the IAA Planetary Defense Conference, Frascati, Roma.

- [6] Walker, R., Izzo, D., de Negueruela, C., Summerer, L., Ayre, M., Vasile, M., 2005. Concepts for Near-Earth Asteroid Deflection using Spacecraft with Advanced Nuclear and Solar Electric Propulsion Systems. *J. Br. Interplanet. Soc.* 58, 268–278.
- [7] Kring, D.A., Boslough, M., 2014. Chelyabinsk: Portrait of an asteroid airburst. *Phys. Today* 67, 32–37. <https://doi.org/10.1063/PT.3.2515>
- [8] ALE3D [WWW Document], n.d. URL <https://ale3d4i.llnl.gov/> (accessed 9.21.23).
- [9] Lubin, P., Cohen, A.N., 2023. Asteroid interception and disruption for terminal planetary defense. *Adv. Space Res.* 71, 1827–1839. <https://doi.org/10.1016/j.asr.2022.10.018>
- [10] PI-Multimodal Planetary Defense, n.d. URL <https://www.deepspace.ucsb.edu/projects/pi-terminal-planetary-defense> (accessed 9.22.23).
- [11] Martin, S., 1965. Diffusion-controlled ignition of cellulosic materials by intense radiant energy. *Symp. Int. Combust., Tenth Symposium (International) on Combustion* 10, 877–896. [https://doi.org/10.1016/S0082-0784\(65\)80232-6](https://doi.org/10.1016/S0082-0784(65)80232-6)
- [12] Glasstone, S., Dolan, P.J., 1977. *The Effects of Nuclear Weapons*. Third edition (No. TID-28061). Department of Defense, Washington, D.C. (USA); Department of Energy, Washington, D.C. (USA). <https://doi.org/10.2172/6852629>
- [13] IAU Minor Planet Center [WWW Document], n.d. URL https://www.minorplanetcenter.net/db_search/show_object?object_id=2023+NT1&commit=Show (accessed 7.21.23).
- [14] Small-Body Database Lookup [WWW Document], n.d. URL https://ssd.jpl.nasa.gov/tools/sbdb_lookup.html#/?sstr=2023%20NT1&view=OPC (accessed 7.21.23).
- [15] Sentry: Earth Impact Monitoring [WWW Document], n.d. URL <https://cneos.jpl.nasa.gov/sentry/details.html#?des=2023%20NT1> (accessed 8.4.23).
- [16] Popova, O.P., Jenniskens, P., Emel’yanenko, V., Kartashova, A., Biryukov, E., Khaibrakhmanov, S., Shuvalov, V., Rybnov, Y., Dudorov, A., Grokhovsky, V.I., Badyukov, D.D., Yin, Q.-Z., Gural, P.S., Albers, J., Granvik, M., Evers, L.G., Kuiper, J., Kharlamov, V., Solovyov, A., Rusakov, Y.S., Korotkiy, S., Serdyuk, I., Korochantsev, A.V., Larionov, M.Yu., Glazachev, D., Mayer, A.E., Gisler, G., Gladkovsky, S.V., Wimpenny, J., Sanborn, M.E., Yamakawa, A., Verosub, K.L., Rowland, D.J., Roeske, S., Botto, N.W., Friedrich, J.M., Zolensky, M.E., Le, L., Ross, D., Ziegler, K., Nakamura, T., Ahn, I., Lee, J.I., Zhou, Q., Li, X.-H., Li, Q.-L., Liu, Y., Tang, G.-Q., Hiroi, T., Sears, D., Weinstein, I.A., Vokhmintsev, A.S., Ishchenko, A.V., Schmitt-Kopplin, P., Hertkorn, N., Nagao, K., Haba, M.K., Komatsu, M., Mikouchi, T., (THE CHELYABINSK AIRBURST CONSORTIUM), 2013. Chelyabinsk Airburst, Damage Assessment, Meteorite Recovery, and Characterization. *Science* 342, 1069–1073. <https://doi.org/10.1126/science.1242642>

- [17] Brown, P., Spalding, R.E., ReVelle, D.O., Tagliaferri, E., Worden, S.P., 2002. The flux of small near-Earth objects colliding with the Earth. *Nature* 420, 294–296. <https://doi.org/10.1038/nature01238>
- [18] Five Years after the Chelyabinsk Meteor: NASA Leads Planetary Defense | NASA [WWW Document], n.d. URL <https://www.nasa.gov/feature/five-years-after-the-chelyabinsk-meteor-nasa-leads-efforts-in-planetary-defense> (accessed 8.7.23).
- [19] Russian Region Begins Recovery In Aftermath Of Meteor Fall [WWW Document], n.d. URL <https://www.wbur.org/news/2013/02/16/russian-meteor-clean-up> (accessed 8.7.23).
- [20] Jenniskens, P., Popova, O.P., Glazachev, D.O., Podobnaya, E.D., Kartashova, A.P., 2019. Tunguska eyewitness accounts, injuries, and casualties. *Icarus* 327, 4–18. <https://doi.org/10.1016/j.icarus.2019.01.001>
- [21] Longo, G., 2007. The Tunguska Event, in: Bobrowsky, P.T., Rickman, H. (Eds.), *Comet/Asteroid Impacts and Human Society: An Interdisciplinary Approach*. Springer, Berlin, Heidelberg, pp. 303–330. https://doi.org/10.1007/978-3-540-32711-0_18
- [22] Harris, A.W., D’Abramo, G., 2015. The population of near-Earth asteroids. *Icarus* 257, 302–312. <https://doi.org/10.1016/j.icarus.2015.05.004>
- [23] Boslough, M.B.E., Crawford, D.A., 2008. Low-altitude airbursts and the impact threat. *Int. J. Impact Eng., Hypervelocity Impact Proceedings of the 2007 Symposium* 35, 1441–1448. <https://doi.org/10.1016/j.ijimpeng.2008.07.053>
- [24] MPEC 2020-G05 : COMET C/2020 F3 (NEOWISE) [WWW Document], n.d. URL <https://minorplanetcenter.net/mpec/K20/K20G05.html> (accessed 8.7.23).
- [25] Horizons System [WWW Document], n.d. URL [https://ssd.jpl.nasa.gov/horizons/app.html/#/](https://ssd.jpl.nasa.gov/horizons/app.html#/) (accessed 9.22.23).
- [26] Lubin, P., Cohen, A.N., 2022. Don’t Forget To Look Up. <https://doi.org/10.48550/arXiv.2201.10663>
- [27] Cheng, A.F., Agrusa, H.F., Barbee, B.W., Meyer, A.J., Farnham, T.L., Raducan, S.D., Richardson, D.C., Dotto, E., Zinzi, A., Della Corte, V., Statler, T.S., Chesley, S., Naidu, S.P., Hirabayashi, M., Li, J.-Y., Eggl, S., Barnouin, O.S., Chabot, N.L., Chocron, S., Collins, G.S., Daly, R.T., Davison, T.M., DeCoster, M.E., Ernst, C.M., Ferrari, F., Graninger, D.M., Jacobson, S.A., Jutzi, M., Kumamoto, K.M., Luther, R., Lyzhoft, J.R., Michel, P., Murdoch, N., Nakano, R., Palmer, E., Rivkin, A.S., Scheeres, D.J., Stickle, A.M., Sunshine, J.M., Trigo-Rodriguez, J.M., Vincent, J.-B., Walker, J.D., Wünnemann, K., Zhang, Y., Amoroso, M., Bertini, I., Brucato, J.R., Capannolo, A., Cremonese, G., Dall’Ora, M., Deshapriya, P.J.D., Gai, I., Hasselmann, P.H., Ieva, S., Impresario, G., Ivanovski, S.L., Lavagna, M., Lucchetti, A., Epifani, E.M., Modenini, D., Pajola, M., Palumbo, P., Perna, D., Pirrotta, S., Poggiali, G., Rossi, A., Tortora, P., Zannoni, M., Zanotti, G., 2023. Momentum transfer from the DART mission kinetic impact on asteroid Dimorphos. *Nature* 616, 457–460. <https://doi.org/10.1038/s41586-023-05878-z>

- [28] Thomas, C.A., Naidu, S.P., Scheirich, P., Moskovitz, N.A., Pravec, P., Chesley, S.R., Rivkin, A.S., Osip, D.J., Lister, T.A., Benner, L.A.M., Brozović, M., Contreras, C., Morrell, N., Rožek, A., Kušnirák, P., Hornoch, K., Mages, D., Taylor, P.A., Seymour, A.D., Snodgrass, C., Jørgensen, U.G., Dominik, M., Skiff, B., Polakis, T., Knight, M.M., Farnham, T.L., Giorgini, J.D., Rush, B., Bellerose, J., Salas, P., Armentrout, W.P., Watts, G., Busch, M.W., Chatelain, J., Gomez, E., Greenstreet, S., Phillips, L., Bonavita, M., Burgdorf, M.J., Khalouei, E., Longa-Peña, P., Rabus, M., Sajadian, S., Chabot, N.L., Cheng, A.F., Ryan, W.H., Ryan, E.V., Holt, C.E., Agrusa, H.F., 2023. Orbital period change of Dimorphos due to the DART kinetic impact. *Nature* 616, 448–451. <https://doi.org/10.1038/s41586-023-05805-2>
- [29] Jewitt, D., Kim, Y., Li, J., Mutchler, M., 2023. The Dimorphos Boulder Swarm. *Astrophys. J. Lett.* 952, L12. <https://doi.org/10.3847/2041-8213/ace1ec>
- [30] Boslough, M., Brown, P., Harris, A., 2015. Updated population and risk assessment for airbursts from near-earth objects (NEOs), in: 2015 IEEE Aerospace Conference. Presented at the 2015 IEEE Aerospace Conference, pp. 1–12. <https://doi.org/10.1109/AERO.2015.7119288>
- [31] Brode, H.L., 1968. Review of Nuclear Weapons Effects. *Annu. Rev. Nucl. Sci.* 18, 153–202. <https://doi.org/10.1146/annurev.ns.18.120168.001101>
- [32] Statler, T.S., Raducan, S.D., Barnouin, O.S., DeCoster, M.E., Chesley, S.R., Barbee, B., Agrusa, H.F., Cambioni, S., Cheng, A.F., Dotto, E., Eggl, S., Fahnestock, E.G., Ferrari, F., Graninger, D., Herique, A., Herreros, I., Hirabayashi, M., Ivanovski, S., Jutzi, M., Karatekin, Ö., Lucchetti, A., Luther, R., Makadia, R., Marzari, F., Michel, P., Murdoch, N., Nakano, R., Ormö, J., Pajola, M., Rivkin, A.S., Rossi, A., Sánchez, P., Schwartz, S.R., Soldini, S., Souami, D., Stickle, A., Tortora, P., Trigo-Rodríguez, J.M., Venditti, F., Vincent, J.-B., Wünnemann, K., 2022. After DART: Using the First Full-scale Test of a Kinetic Impactor to Inform a Future Planetary Defense Mission. *Planet. Sci. J.* 3, 244. <https://doi.org/10.3847/PSJ/ac94c1>

Appendix

I. Tables

Table 1. Summary of mitigated (fragmented) 2023 NT1 threat scenarios and estimated ground effects. All scenarios assume a spherical parent asteroid with impact speed of 15.59 km/s. D indicates parent asteroid diameter; $\bar{\rho}$ indicates parent asteroid average density.

Case	D (m)	$\bar{\rho}$ (kg/m ³)	Entry angle (°)	No. fragments	Avg. fragment size (m)	Intercept time	Unbroken exo-atm. energy (Mt)	1% optical CDF value (J/m ²)	Weighted avg. optical energy (J/m ²)	1% acoustic CDF value (Pa)	Weighted avg. pressure (Pa)
1	26	2600	45	1000	2.60	1 d	6.95E-01	1.11E+03	4.06E+02	3.70E+02	1.47E+02
2	26	2600	45	1000	2.60	10 d	6.95E-01	4.74E+01	1.11E+01	1.49E+02	4.47E+01
3	26	2600	45	1000	2.60	12 hr	6.95E-01	3.13E+03	1.34E+03	5.86E+02	2.69E+02
4	26	2600	45	4000	1.64	1 d	6.95E-01	7.92E+02	2.82E+02	4.52E+02	1.77E+02
5	26	2600	45	4000	1.64	10 d	6.95E-01	1.82E+01	4.84E+00	1.15E+02	3.62E+01

2023 NT1 – A Cautionary Tale

Table 1. Summary of mitigated (fragmented) 2023 NT1 threat scenarios and estimated ground effects. All scenarios assume a spherical parent asteroid with impact speed of 15.59 km/s. D indicates parent asteroid diameter; $\bar{\rho}$ indicates parent asteroid average density.

Case	D (m)	$\bar{\rho}$ (kg/m ³)	Entry angle (°)	No. fragments	Avg. fragment size (m)	Intercept time	Unbroken exo-atm. energy (Mt)	1% optical CDF value (J/m ²)	Weighted avg. optical energy (J/m ²)	1% acoustic CDF value (Pa)	Weighted avg. pressure (Pa)
6	26	2600	45	4000	1.64	12 hr	6.95E-01	2.44E+03	9.05E+02	8.66E+02	3.95E+02
7	30	1400	45	1000	3.00	1 d	5.75E-01	7.31E+02	2.39E+02	3.00E+02	1.14E+02
8	30	2600	20	1000	3.00	1 d	1.07E+00	1.69E+03	6.39E+02	3.78E+02	1.50E+02
9	30	2600	45	1000	3.00	1 d	1.07E+00	2.04E+03	7.75E+02	4.38E+02	1.76E+02
10	30	2600	45	1000	3.00	1 hr	1.07E+00	1.36E+04	8.32E+03	1.76E+03	9.81E+02
11	30	2600	70	1000	3.00	1 d	1.07E+00	2.29E+03	8.58E+02	4.76E+02	1.92E+02
12	30	2600	90	1000	3.00	1 d	1.07E+00	2.38E+03	8.74E+02	4.80E+02	1.94E+02
13	30	4800	45	1000	3.00	1 d	1.97E+00	6.71E+03	2.53E+03	7.73E+02	2.91E+02
14	30	6000	45	2000	2.38	1 d	2.46E+00	1.14E+04	4.18E+03	1.11E+03	3.81E+02
15	34	1400	45	1000	3.40	1 d	8.37E-01	1.19E+03	4.46E+02	3.48E+02	1.47E+02
16	34	2600	20	1000	3.40	1 d	1.55E+00	2.97E+03	1.13E+03	4.36E+02	1.77E+02
17	34	2600	45	1000	3.40	1 d	1.55E+00	3.47E+03	1.30E+03	5.05E+02	1.98E+02
18	34	2600	70	1000	3.40	1 d	1.55E+00	3.78E+03	1.42E+03	5.49E+02	2.16E+02
19	34	2600	90	1000	3.40	1 d	1.55E+00	3.80E+03	1.48E+03	5.58E+02	2.18E+02
20	34	2600	45	1000	3.40	10 d	1.55E+00	1.42E+02	3.42E+01	2.16E+02	6.55E+01
21	34	2600	45	1000	3.40	12 hr	1.55E+00	8.98E+03	4.22E+03	7.97E+02	3.68E+02
22	34	2600	45	4000	2.14	1 d	1.55E+00	1.95E+03	7.04E+02	5.32E+02	2.02E+02
23	34	2600	45	4000	2.14	10 d	1.55E+00	5.13E+01	1.37E+01	1.44E+02	4.62E+01
24	34	2600	45	4000	2.14	12 hr	1.55E+00	5.56E+03	2.27E+03	9.77E+02	4.47E+02
25	34	4000	45	1000	3.40	1 d	2.39E+00	7.77E+03	2.99E+03	7.44E+02	2.78E+02
26	34	6000	45	1000	3.40	1 d	3.59E+00	2.12E+04	7.78E+03	1.28E+03	4.49E+02
27	35	1800	45	1000	3.50	1 d	1.17E+00	1.94E+03	7.67E+02	4.10E+02	1.63E+02
28	35	2600	20	1000	3.50	1 d	1.70E+00	3.42E+03	1.28E+03	4.53E+02	1.84E+02
29	35	2600	45	1000	3.50	1 d	1.70E+00	3.42E+03	1.28E+03	4.53E+02	1.84E+02
30	35	2600	70	1000	3.50	1 d	1.70E+00	4.42E+03	1.66E+03	5.77E+02	2.27E+02
31	35	2600	90	1000	3.50	1 d	1.70E+00	4.70E+03	1.72E+03	5.96E+02	2.23E+02
32	35	4000	45	1000	3.50	1 d	2.61E+00	9.40E+03	3.43E+03	7.81E+02	2.95E+02
33	35	6000	45	2000	2.78	1 d	3.91E+00	1.94E+04	7.08E+03	1.27E+03	4.60E+02
34	40	2600	20	1000	4.00	1 d	2.53E+00	5.28E+03	2.06E+03	5.25E+02	2.13E+02
35	40	2600	45	1000	4.00	1 d	2.53E+00	5.28E+03	2.06E+03	5.25E+02	2.13E+02
36	40	2600	70	1000	4.00	1 d	2.53E+00	7.52E+03	2.86E+03	6.90E+02	2.67E+02

2023 NT1 – A Cautionary Tale

Table 1. Summary of mitigated (fragmented) 2023 NT1 threat scenarios and estimated ground effects. All scenarios assume a spherical parent asteroid with impact speed of 15.59 km/s. D indicates parent asteroid diameter; $\bar{\rho}$ indicates parent asteroid average density.

Case	D (m)	$\bar{\rho}$ (kg/m ³)	Entry angle (°)	No. fragments	Avg. fragment size (m)	Intercept time	Unbroken exo-atm. energy (Mt)	1% optical CDF value (J/m ²)	Weighted avg. optical energy (J/m ²)	1% acoustic CDF value (Pa)	Weighted avg. pressure (Pa)
37	40	2600	90	1000	4.00	1 d	2.53E+00	7.49E+03	2.86E+03	7.00E+02	2.71E+02
38	40	2700	45	1000	4.00	1 d	2.63E+00	6.62E+03	2.64E+03	6.35E+02	2.58E+02
39	40	3400	45	1000	4.00	1 d	3.31E+00	1.15E+04	4.16E+03	7.80E+02	3.09E+02
40	40	6000	45	2000	3.17	1 d	5.84E+00	3.16E+04	1.17E+04	1.47E+03	5.39E+02
41	45	2600	20	1000	4.50	1 d	3.60E+00	7.99E+03	3.18E+03	5.90E+02	2.37E+02
42	45	2600	45	1000	4.50	1 d	3.60E+00	7.99E+03	3.18E+03	5.90E+02	2.37E+02
43	45	2600	70	1000	4.50	1 d	3.60E+00	1.17E+04	4.50E+03	7.95E+02	3.11E+02
44	45	2600	90	1000	4.50	1 d	3.60E+00	1.13E+04	4.44E+03	8.01E+02	3.22E+02
45	45	2800	45	1000	4.50	1 d	3.88E+00	1.24E+04	4.73E+03	7.69E+02	2.95E+02
46	45	4000	45	1000	4.50	1 d	5.54E+00	2.53E+04	9.05E+03	1.05E+03	4.05E+02
47	45	4000	45	1000	4.50	12 hr	5.54E+00	5.71E+04	2.68E+04	1.62E+03	7.06E+02
48	45	4000	45	1000	4.50	1 hr	5.54E+00	1.84E+05	9.50E+04	4.62E+03	2.40E+03
49	45	6000	45	4000	2.83	1 d	8.31E+00	4.42E+04	1.63E+04	1.75E+03	6.09E+02
50	50	2600	20	1000	5.00	1 d	4.94E+00	1.39E+04	5.36E+03	7.02E+02	2.85E+02
51	50	2600	45	1000	5.00	1 d	4.94E+00	1.39E+04	5.36E+03	7.02E+02	2.85E+02
52	50	2600	70	1000	5.00	1 d	4.94E+00	1.39E+04	5.36E+03	7.02E+02	2.85E+02
53	50	2600	90	1000	5.00	1 d	4.94E+00	1.39E+04	5.36E+03	7.02E+02	2.85E+02
54	50	3100	45	1000	5.00	1 d	5.89E+00	2.26E+04	8.59E+03	9.65E+02	3.53E+02
55	50	4500	45	2000	5.00	1 d	8.55E+00	3.52E+04	1.34E+04	1.28E+03	4.66E+02
56	50	6000	45	4000	3.15	1 d	1.14E+01	6.10E+04	2.30E+04	1.92E+03	6.75E+02
57	50	6000	45	4000	3.15	2 d	1.14E+01	2.15E+04	7.10E+03	1.20E+03	3.64E+02
58	55	2600	20	1000	5.50	1 d	6.58E+00	1.72E+04	7.23E+03	7.60E+02	3.16E+02
59	55	2600	20	2000	5.50	1 d	6.58E+00	1.84E+04	7.26E+03	8.96E+02	3.45E+02
60	55	2600	45	1000	5.50	1 d	6.58E+00	2.22E+04	8.81E+03	9.41E+02	3.76E+02
61	55	2600	45	2000	5.50	1 d	6.58E+00	1.84E+04	7.26E+03	8.96E+02	3.45E+02
62	55	2600	70	1000	5.50	1 d	6.58E+00	2.68E+04	1.03E+04	1.05E+03	4.08E+02
63	55	2600	70	2000	5.50	1 d	6.58E+00	1.84E+04	7.26E+03	8.96E+02	3.45E+02
64	55	2600	90	1000	5.50	1 d	6.58E+00	2.81E+04	1.08E+04	1.09E+03	4.04E+02
65	55	2600	90	2000	5.50	1 d	6.58E+00	1.84E+04	7.26E+03	8.96E+02	3.45E+02
66	55	3800	45	2000	5.50	1 d	9.61E+00	3.56E+04	1.37E+04	1.20E+03	4.49E+02
67	55	6000	45	4000	3.46	1 d	1.52E+01	8.77E+04	3.31E+04	2.14E+03	7.61E+02

2023 NT1 – A Cautionary Tale

Table 1. Summary of mitigated (fragmented) 2023 NT1 threat scenarios and estimated ground effects. All scenarios assume a spherical parent asteroid with impact speed of 15.59 km/s. D indicates parent asteroid diameter; $\bar{\rho}$ indicates parent asteroid average density.

Case	D (m)	$\bar{\rho}$ (kg/m ³)	Entry angle (°)	No. fragments	Avg. fragment size (m)	Intercept time	Unbroken exo-atm. energy (Mt)	1% optical CDF value (J/m ²)	Weighted avg. optical energy (J/m ²)	1% acoustic CDF value (Pa)	Weighted avg. pressure (Pa)
68	55	6000	45	4000	3.46	2 d	1.52E+01	2.82E+04	9.51E+03	1.33E+03	4.02E+02
69	55	6000	45	6000	3.03	1 d	1.52E+01	7.94E+04	3.00E+04	2.16E+03	7.52E+02
70	55	6000	45	6000	3.03	2 d	1.52E+01	2.64E+04	9.12E+03	1.32E+03	3.98E+02
71	58	1400	45	1000	5.80	1 d	4.15E+00	1.20E+04	4.72E+03	7.28E+02	2.97E+02
72	58	2600	20	1000	5.80	1 d	7.71E+00	2.13E+04	8.60E+03	8.18E+02	3.27E+02
73	58	2600	45	1000	5.80	1 d	7.71E+00	2.87E+04	1.12E+04	1.03E+03	3.82E+02
74	58	2600	70	1000	5.80	1 d	7.71E+00	3.26E+04	1.29E+04	1.13E+03	4.13E+02
75	58	2600	90	1000	5.80	1 d	7.71E+00	3.47E+04	1.25E+04	1.16E+03	4.51E+02
76	58	2600	45	1000	5.80	10 d	7.71E+00	1.19E+03	2.80E+02	4.54E+02	1.32E+02
77	58	2600	45	1000	5.80	12 hr	7.71E+00	7.51E+04	3.58E+04	1.61E+03	7.17E+02
78	58	2600	45	4000	3.65	1 d	7.71E+00	1.81E+04	7.18E+03	9.49E+02	3.68E+02
79	58	2600	45	4000	3.65	10 d	7.71E+00	4.61E+02	1.37E+02	2.78E+02	8.91E+01
80	58	2600	45	4000	3.65	12 hr	7.71E+00	4.60E+04	2.20E+04	1.67E+03	7.75E+02
81	58	4000	45	1000	5.80	1 d	1.19E+01	6.65E+04	2.42E+04	1.48E+03	5.36E+02
82	58	6000	45	1000	5.80	1 d	1.78E+01	1.46E+05	5.40E+04	2.38E+03	8.69E+02
83	58	6000	45	1000	5.80	1 d	1.78E+01	1.05E+05	3.95E+04	2.25E+03	7.97E+02
84	58	6000	45	1000	5.80	2 d	1.78E+01	3.50E+04	1.17E+04	1.40E+03	4.23E+02
85	60	1400	45	2000	4.37	1 d	4.60E+00	9.86E+03	3.96E+03	7.01E+02	2.82E+02
86	60	1400	45	4000	3.78	2 d	4.60E+00	2.68E+03	9.13E+02	4.23E+02	1.32E+02
87	60	2600	20	1000	6.00	1 d	8.54E+00	2.57E+04	1.07E+04	8.63E+02	3.61E+02
88	60	2600	20	4000	3.78	2 d	8.54E+00	5.90E+03	2.08E+03	5.12E+02	1.60E+02
89	60	2600	45	1000	6.00	1 d	8.54E+00	3.11E+04	1.22E+04	1.04E+03	4.23E+02
90	60	2600	45	4000	3.78	2 d	8.54E+00	7.36E+03	2.52E+03	6.05E+02	1.87E+02
91	60	2600	70	1000	6.00	1 d	8.54E+00	3.38E+04	1.35E+04	1.15E+03	4.62E+02
92	60	2600	70	4000	3.78	2 d	8.54E+00	5.90E+03	2.08E+03	5.12E+02	1.60E+02
93	60	2600	90	1000	6.00	1 d	8.54E+00	3.76E+04	1.48E+04	1.22E+03	3.81E+02
94	60	2600	90	4000	3.78	2 d	8.54E+00	5.90E+03	2.08E+03	5.12E+02	1.60E+02
95	60	3200	45	4000	3.78	2 d	1.05E+01	1.03E+04	3.54E+03	7.09E+02	2.16E+02
96	60	4500	45	4000	3.78	2 d	1.48E+01	2.04E+04	6.98E+03	9.78E+02	2.99E+02
97	60	4500	45	6000	3.30	2 d	1.48E+01	1.79E+04	6.19E+03	9.62E+02	2.94E+02
98	60	5200	45	4000	3.78	2 d	1.71E+01	2.77E+04	9.53E+03	1.18E+03	3.61E+02

2023 NT1 – A Cautionary Tale

Table 1. Summary of mitigated (fragmented) 2023 NT1 threat scenarios and estimated ground effects. All scenarios assume a spherical parent asteroid with impact speed of 15.59 km/s. D indicates parent asteroid diameter; $\bar{\rho}$ indicates parent asteroid average density.

Case	D (m)	$\bar{\rho}$ (kg/m ³)	Entry angle (°)	No. fragments	Avg. fragment size (m)	Intercept time	Unbroken exo-atm. energy (Mt)	1% optical CDF value (J/m ²)	Weighted avg. optical energy (J/m ²)	1% acoustic CDF value (Pa)	Weighted avg. pressure (Pa)
99	60	5200	45	6000	3.30	2 d	1.71E+01	2.42E+04	8.44E+03	1.16E+03	3.50E+02
100	60	6000	45	6000	3.30	1 d	1.97E+01	1.10E+05	4.15E+04	2.38E+03	8.60E+02
101	60	6000	45	6000	3.30	2 d	1.97E+01	3.55E+04	1.21E+04	1.42E+03	4.34E+02
102	60	7000	45	4000	3.78	2 d	2.30E+01	6.15E+04	2.05E+04	1.94E+03	5.87E+02
103	60	7000	45	4000	3.78	5 d	2.30E+01	1.25E+04	3.71E+03	1.37E+03	4.22E+02

Table 2. Summary of unmitigated (unfragmented) 2023 NT1 threat scenarios and estimated ground effects. All scenarios assume a spherical parent asteroid with impact speed of 15.59 km/s and entry angle of 45°. D indicates parent asteroid diameter; $\bar{\rho}$ indicates parent asteroid average density. Note that the maximum optical energy and maximum pressure values are experienced at the lowest probability level of the simulation, which may vary between cases.

Case	D (m)	$\bar{\rho}$ (kg/m ³)	Entry angle (°)	Unbroken exo-atm. energy (Mt)	1% optical CDF value (J/m ²)	Weighted avg. optical energy (J/m ²)	Max. optical energy observed (J/m ²)	1% acoustic CDF value (Pa)	Weighted avg. pressure (Pa)	Max. pressure observed (Pa)
104	26	2600	45	6.95E-01	9.42E+04	2.26E+04	1.05E+05	2.89E+03	1.20E+03	3.03E+03
105	30	2600	45	1.07E+00	1.90E+05	4.39E+04	2.18E+05	3.79E+03	9.55E+02	4.04E+03
106	34	2600	45	1.55E+00	3.57E+05	8.02E+04	4.23E+05	4.87E+03	1.16E+03	5.30E+03
107	34	4000	45	2.39E+00	1.03E+06	2.21E+05	1.39E+06	7.87E+03	1.61E+03	9.26E+03
108	34	6000	45	3.59E+00	3.80E+06	9.92E+05	9.02E+06	1.62E+04	2.95E+03	3.18E+04
109	35	2600	45	1.70E+00	4.12E+05	9.25E+04	4.95E+05	5.21E+03	1.22E+03	5.66E+03
110	40	2600	45	2.53E+00	8.29E+05	1.81E+05	1.05E+06	6.91E+03	1.53E+03	7.86E+03
111	45	2600	45	3.60E+00	1.56E+06	3.38E+05	2.10E+06	9.21E+03	1.90E+03	1.10E+04
112	45	4000	45	5.54E+00	4.73E+06	1.11E+06	8.73E+06	1.69E+04	3.01E+03	2.65E+04
113	50	2600	45	4.94E+00	2.83E+06	6.10E+05	4.08E+06	1.24E+04	2.36E+03	1.56E+04
114	50	4500	45	8.55E+00	1.20E+07	3.56E+06	3.75E+07	3.03E+04	6.21E+03	9.17E+04
115	55	2600	45	6.58E+00	4.78E+06	1.08E+06	7.81E+06	1.63E+04	2.98E+03	2.32E+04
116	58	2600	45	7.71E+00	6.54E+06	1.50E+06	1.14E+07	1.96E+04	3.47E+03	3.02E+04
117	58	4000	45	1.19E+01	1.99E+07	6.66E+06	8.28E+07	4.20E+04	1.10E+04	2.00E+05
118	58	6000	45	1.78E+01	6.45E+07	4.11E+07	2.15E+09	2.89E+05	2.18E+05	1.45E+07
119	60	2600	45	8.54E+00	7.88E+06	1.87E+06	1.48E+07	2.19E+04	3.88E+03	3.66E+04
120	60	5200	45	1.71E+01	1.94E+08	1.18E+08	9.69E+09	2.74E+06	1.52E+06	1.37E+08